

Chiral Discrimination on Gate-Based Quantum Computers

Muhammad Arsalan Ali Akbar^{1,2,*} and Sabre Kais^{1,2,*}

¹*Department of Electrical and Computer Engineering, North Carolina State University, Raleigh, NC 27606*

²*Department of Chemistry, North Carolina State University, Raleigh, North Carolina 27695*

We present a novel approach to chiral discrimination using gate-based quantum processors, addressing a key challenge in adapting conventional control techniques using modern quantum computing. Schemes such as stimulated rapid adiabatic passage (STIRAP) and shortcuts to adiabaticity (STAP) have shown strong potential for enantiomer discrimination; their reliance on analog and continuous-time control makes them incompatible with digital gate-based quantum computing architectures. Here, we adapt these protocols for quantum computers by discretizing their Gaussian-shaped pulses through Trotterization. We simulate the chiral molecule 1,2-propanediol and experimentally validate this gate-based implementation on IBM quantum hardware. Our results demonstrate that this approach is a viable foundation for advancing chiral discrimination protocols, preparing the way for quantum-level manipulation of molecular chirality on accessible quantum architectures.

I. INTRODUCTION

Understanding and harnessing light-matter interactions is essential to addressing a wide range of complex challenges in modern science and engineering. Over the last two decades, scientists have developed different techniques to rigorously control its phase, amplitude, and spatial distribution, enabling the study of this interaction at the molecular level [1–5]. For instance, these methods are crucial to understanding chirality. This intrinsic property arises when an object cannot superimpose onto its mirror image, and these mirror images are called enantiomers [6, 7]. From dark clouds to the early Earth ages, nature has paraded a unique preference for certain chirality forms, selecting L-amino acids as building blocks of proteins and enzymes, while favoring D-sugars as key components of DNA and RNA [8]. In addition to biology, chirality is a universal phenomenon ranging from subatomic particles, such as neutrinos, to supra-molecular assemblies and even interstellar medium, comets, and meteorites [9–11]. This ubiquitous occurrence of chirality shows how critical it is to study its origin, implications, and applications in biological and physical sciences. The tragedy of thalidomide [12] in the late 1950s and early 1960s shows how important the precise control of chiral discrimination is in medicines, since one enantiomer of thalidomide caused severe congenital disabilities, whereas the other exhibited therapeutic effects.

Traditional separation methods, such as crystallization or distillation, did not work because the two enantiomers of chiral molecules exhibit identical physical properties, such as melting points, boiling points, and densities. As a result, their discrimination and purification remain a formidable task [13]. Researchers have proposed various spectroscopic techniques to address these challenges, employing external auxiliary fields to mediate the interaction with specific enantiomers. These techniques measure the absorption difference between L and R enantiomers by probing chiral perturbation, detect vibrational optical activity via inelastic scattering, or utilize chiral-induced spin selectivity [14–17]. However, many techniques often require concentrated samples and long acquisition

times, which can be challenging to achieve in an experimental setup.

Because chiral molecules cannot be superimposed, this asymmetry allows for unique quantum mechanical behaviors, particularly in their interaction with light. In the traditional Raman process [18, 19], a sequence of three-state transitions leads to a final state that differs from the initial state through radiative excitation followed by spontaneous emission. However, the adiabatic passage technique enables complete population transfer between quantum states through an intermediate state while bypassing spontaneous decay. In particular, Stimulated Raman Adiabatic Passage (STIRAP) [20–22] involves a three-level configuration in which the broken symmetry of the chiral molecules allows microwave-driven rotational transitions (one-photon process) and Raman-like transitions via virtual intermediate states (two-photon process). In this cyclic population transfer (CPT), the STIRAP sequence ($|1\rangle \rightarrow |3\rangle$ via $|2\rangle$), combined with a direct ($|1\rangle \rightarrow |3\rangle$) drive, created a chiral-selective population configuration. These two paths cancel out in the presence of inversion symmetry, but in a chiral molecule, the configuration remains open due to broken parity rules. Consequently, the triple product of the dipole moment components, which emerges during state transitions, has opposite signs for the enantiomers, enabling their discrimination [23, 24].

The adiabatic passage (AP) is robust against parameter fluctuations and decoherence, but its adiabatic criterion requires a long evolution time. Therefore, researchers focus on developing shortcuts to adiabatic passage (STAP) [25–27] that tailor the time-dependent Hamiltonian to enable faster evolution while preserving adiabaticity. Different methods have been proposed to speed up AP, such as iterative interaction pictures, transitionless quantum driving, and invariant-based inverse engineering. However, the basic idea is to add counteradiabatic terms [28] to the STIRAP Hamiltonian to suppress nonadiabatic transitions, and to shape the pulse time dependence so the system follows invariant eigenstates, thereby reaching the required final state. In various cases, the integration of both ideas has enabled more effective experimental implementations of STAP.

An interesting aspect of STAP is its potential to translate into quantum gate operations, opening new possibilities for

* skais@ncsu.edu

efficient population transfer in more intricate quantum systems. In recent years, STIRAP and STAP protocols have been explored and experimentally realized for transferring quantum states between transmon superconducting qubits [29–31], and have also been demonstrated to speed up adiabatic transitions in three-level transmon circuits. Although STIRAP and shortcuts to adiabaticity (STAP) have been proven effective for population transfer of enantiomers in chiral systems, their implementation typically depends on analog pulse shapes and precise timing, which makes them difficult to realize on gate-based quantum computers that rely on discrete operations rather than continuous driving fields. Recent work has shown that, within a trapped-ion-based quantum simulator, a chiral system subjected to dipole interactions undergoes cyclic time evolution, accumulating a chirality-dependent non-Abelian geometric phase. The resulting phase difference serves as a robust mechanism for enantiomer discrimination. [32]. However, preparing an initial state for a large chiral molecule using laser cooling and addressing the rotational states with a microwave pulse is still an open question. To bridge this gap, we adapt the core mechanism of these protocols onto equivalent quantum circuits, which makes them compatible with the inherent nature of current quantum devices.

In this work, we introduce a new direction for studying and controlling enantiomers at the quantum level by mapping the rotational energy levels of asymmetric top molecules onto a qubit basis. To represent the three-level Hamiltonian $H_{int}(t)$ with qubits, we consider two qubits with a basis set $\{|00\rangle, |01\rangle, |10\rangle, |11\rangle\}$. We implement the time evolution of the Gaussian Q -pulse in the quantum circuit using Trotterization, where the phase signatures of L and R enantiomers are encoded in the rotation gates at each step. Once the Q -pulse is encoded, the P - and S -pulses are implemented by approximating their Gaussian envelopes using step-wise Trotterization. We implemented the STIRAP protocol on the state-vector simulator and two IBM quantum devices (ibm_kingston and ibm_fez) and benchmarked against exact diagonalization results, with high fidelity using just 20 discrete time steps. STIRAP requires long evolution times to achieve adiabatic state transfer, thereby reducing the scheme's efficiency. We address this constraint through STAP, where engineered pulse shapes enable rapid and efficient state preparation with improved nonadiabatic population transfer. Its gate-based implementation on IBM quantum devices reproduces high-fidelity results, allowing fast and efficient chiral discrimination with a substantial time advantage over the STIRAP protocol.

II. STIMULATED RAMAN ADIABATIC PASSAGES (STIRAP)

Asymmetric molecules exist in two mirror-image forms, known as L and R enantiomers, as shown in Fig. 1. The three rotational energy levels $|Jmk\rangle$ for an asymmetric top are labeled $\{|1\rangle, |2\rangle, |3\rangle\}$, which are connected in a close configuration. An external electric field drives transitions between these energy levels: $\vec{E}_i(t) = \hat{e}_i \alpha_i \cos(\omega_i t + \phi_i)$ where α_i , ω_i , ϕ_i , and \hat{e}_i are the amplitude, angular frequency,

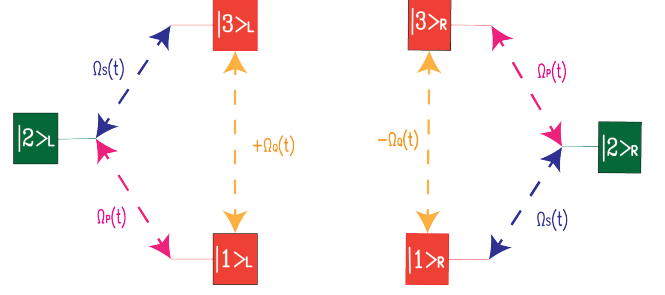


FIG. 1. Closed-loop coupling scheme between three discrete energy states for L and R enantiomers. The Rabi frequencies $\Omega_P(t)$, $\Omega_S(t)$, and $\Omega_Q(t)$ correspond to the P -, S -, and Q -pulses, respectively.

phase, and polarization unit vector, respectively. The interaction between the electric field and the molecular dipole moment is given as $\Omega_{ij}(t) = \vec{\mu}_{ij} \cdot \vec{E}_i(t)$, where $\vec{\mu}_{ij}$ denotes the dipole moment associated with the transition $ij \in \{1, 2, 3\}$. For both enantiomers, the electric field drives the $|1\rangle \leftrightarrow |2\rangle$ and $|2\rangle \leftrightarrow |3\rangle$ transitions with couplings $\Omega_P(t)$ and $\Omega_S(t)$ respectively. However, the $|1\rangle \leftrightarrow |3\rangle$ transition is characterized by $\Omega_Q(t) = \pm \vec{\mu}_{13} \cdot \vec{E}_i(t)$, where the sign difference arises from the opposite dipole moments inherent to chirality.

Then the Hamiltonian is given as

$$H(t) = H_0(t) + H_1(t) \quad (1)$$

where $H_0 = \hbar\omega_{12}|2\rangle\langle 2| + \hbar\omega_{13}|3\rangle\langle 3|$ with $|1\rangle$ as the ground state (zero energy reference state). The electric field interacts with the dipole moment as

$$H_1(t) = \sum_{j>i} \vec{\mu}_{ij} \cdot \vec{E}_i(t) \quad (2)$$

where $\vec{\mu}_{12} = \vec{\mu}_P \cdot \vec{E}_P$, $\vec{\mu}_{23} = \vec{\mu}_S \cdot \vec{E}_S$ and $\vec{\mu}_{13} = \pm \vec{\mu}_Q \cdot \vec{E}_Q$. The Hamiltonian $H_1(t)$ becomes

$$H_1(t) = \left[\vec{\mu}_P \cdot \vec{E}_P (|1\rangle\langle 2| + |2\rangle\langle 1|) + \vec{\mu}_S \cdot \vec{E}_S (|2\rangle\langle 3| + |3\rangle\langle 2|) \pm \vec{\mu}_Q \cdot \vec{E}_Q (|1\rangle\langle 3| + |3\rangle\langle 1|) \right] \quad (3)$$

The total Hamiltonian can be presented as a matrix with basis vectors $\{|1\rangle, |2\rangle, |3\rangle\}$

$$H(t) = \begin{pmatrix} 0 & \vec{\mu}_P \cdot \vec{E}_P & \pm \vec{\mu}_Q \cdot \vec{E}_Q \\ \vec{\mu}_P \cdot \vec{E}_P & \omega_{12} & \vec{\mu}_S \cdot \vec{E}_S \\ \pm \vec{\mu}_Q \cdot \vec{E}_Q & \vec{\mu}_S \cdot \vec{E}_S & \omega_{13} \end{pmatrix} \quad (4)$$

On the other hand, $\Omega_Q(t)$ has opposite signs for L and R enantiomers ($\Omega_Q^L(t) = -\Omega_Q^R(t)$) for chiral molecules.

To simplify the calculations, we transform the Hamiltonian $H(t)$ to the interaction picture and apply the Rotating Wave Approximation (RWA), assuming that the driving field is close to resonance. The Hamiltonian in the interaction picture $H_{\text{int}}(t)$ (see Appendix A for details)

$$H_Q(t_i) = e^{iH_0 t_i} H_1(t_i) e^{-iH_0 t_i} \quad (5)$$

Substituting $H_0(t)$ and $H_1(t)$, the Hamiltonian matrix in the three basis becomes

$$H_{\text{int}}(t) = \frac{1}{2} \begin{pmatrix} 0 & \Omega_P e^{i\phi_P} & \pm \Omega_Q e^{i\phi_Q} \\ \Omega_P e^{-i\phi_P} & 0 & \Omega_S e^{i\phi_S} \\ \pm \Omega_Q e^{-i\phi_Q} & \Omega_S e^{-i\phi_S} & 0 \end{pmatrix} \quad (6)$$

III. QUBITS MAPPING

A. Q -pulse gate

The three-level Hamiltonian $H_{\text{int}}(t)$ is embedded in a two-qubit Hilbert space spanned by the basis states $\{|00\rangle, |01\rangle, |10\rangle, |11\rangle\}$. In this mapping, the logical states are assigned as $|1\rangle = |00\rangle$, $|2\rangle = |11\rangle$, and $|3\rangle = |10\rangle$, while $|01\rangle$ is designated as a leakage state that may become populated through non-adiabatic effects (see Appendix B for details).

The Hamiltonian for Q -pulse only is

$$H_{\text{int}}(t) = \pm \frac{\Omega_Q(t)}{2} [e^{i\phi_Q} |00\rangle\langle 10| + e^{-i\phi_Q} |10\rangle\langle 00|] \quad (7)$$

Here, the Q -pulse is defined as: $\Omega_Q(t) = \Omega_0 e^{-(t-t_f/2)^2/T_q^2}$, where Ω_0 and T_q denote the peak amplitude and temporal width of the Gaussian profile, respectively. The phase ϕ_Q distinguishes the two enantiomers, taking the value $+\frac{\pi}{2}$ for the L-enantiomer and $-\frac{\pi}{2}$ for the R-enantiomer. The first stage starts at $t = 0$ and ends at the time $t = t_f$ to cover the full pulse area. In the quantum circuit, the Gaussian profile of the Q -pulse is simulated via Trotterized time evolution, where the Hamiltonian $H_Q(t_i)$ is applied in discrete intervals: $U_Q^{(i)} = e^{-i(H_Q(t_i)\delta t)}$. At each small step δt the instantaneous Rabi frequency $\Omega_Q(t_i)$ determines the rotation angle ($\theta_i = \Omega_Q(t_i)\delta t$) for the $R_z(\theta_i)$ gate as shown in the Fig. 2. However, the quantum circuit ($CX-R_z-CX$) confines the rotation to the $|00\rangle \leftrightarrow |10\rangle$ transition, and by applying these gates with time-dependent θ_i , the evolution of a continuous Gaussian pulse is approximated. The total time evolution for Q -pulse using the first-order Trotter becomes

$$U_Q^{(i)} = \prod_{i=1}^k e^{-iH_Q(t_i)\delta t} \quad (8)$$

When Q -pulse is fully applied, the initial state of the L and R enantiomers is driven from $|00\rangle$ to $|\Psi\rangle_L = \frac{1}{\sqrt{2}}(|00\rangle_L -$

$|10\rangle_L)$ and $|\Psi\rangle_R = \frac{1}{\sqrt{2}}(|00\rangle_R + |10\rangle_R)$ respectively, as shown in Fig. 5.

B. P - and S -pulse gate

The next step is to apply the pump pulse $\Omega_P(t)$ and stoke pulse $\Omega_S(t)$, which ultimately leads to the discrimination between the L and R enantiomers. In the interaction picture, one gives the Hamiltonian as

$$H_{PS}(t_i) = \frac{1}{2} \left[\Omega_P e^{i\phi_P} |00\rangle\langle 11| + \Omega_P e^{-i\phi_P} |11\rangle\langle 00| + \Omega_S e^{i\phi_S} |11\rangle\langle 10| + \Omega_S e^{-i\phi_S} |10\rangle\langle 11| \right] \quad (9)$$

Here, the resonant conditions are defined as: $\omega_{00 \leftrightarrow 11} - \omega_{00 \leftrightarrow 10} = \omega_{11 \leftrightarrow 10} = \omega_S$ and $\omega_{00 \leftrightarrow 11} = \omega_P$. The time-dependent pump field is modeled as a double Gaussian profile, while a single Gaussian profile represents the Stokes field.

$$\begin{aligned} \Omega_P(t) &= \Omega_0 \exp \left[-\frac{(t-t_1) - (t_f - t_1 - \tau)/2)^2}{T_q^2} \right] \\ &+ \Omega_0 \exp \left[-\frac{(t-t_1) - (t_f - t_1 + \tau)/2)^2}{T_q^2} \right], \quad (10) \\ \Omega_S(t) &= \Omega_0 \exp \left[-\frac{(t-t_1) - (t_f - t_1 - \tau)/2)^2}{T_q^2} \right] \end{aligned}$$

Here, Ω_0 and T_q denote the Gaussian profiles' peak amplitude and temporal width, respectively. The τ specifies the time delay between the two Gaussian components of $\Omega_P(t)$. The pulse shapes are not unique; what is primarily important is the adiabatic conditions ($\dot{\theta} \ll \Omega(t)$) they must satisfy between the energy levels.

The time evolution of the Gaussian profile of the P - and S -pulse is encoded in the quantum circuit through Trotterization, in which we implement $H_{PS}(t_i)$ digitally in small Trotter steps with a discretized Gaussian pulse envelope. Applying Trotterization of $U_{PS}^{(i)} = e^{-i(H_{PS}(t_i)\delta t)}$, the P -pulse collectively generates transitions between $00 \leftrightarrow 11$ with amplitude $\Omega_P(t)$ and this amplitude is encoded in the quantum circuit through controlled single rotational gates R_x with rotational angle $\theta_i = \Omega_P(t_i)\delta t$ as shown in the Fig. 2.

The total time evolution for P -pulse and S -pulse using first-order Trotter as

$$U_{PS}^{(i)} = \prod_{i=1}^{m-k} e^{-i(H_{PS}(t_i)\delta t)}$$

k is the total number of steps, m is the number of steps for which the Q -pulse acts. At the end of the total time evolution,

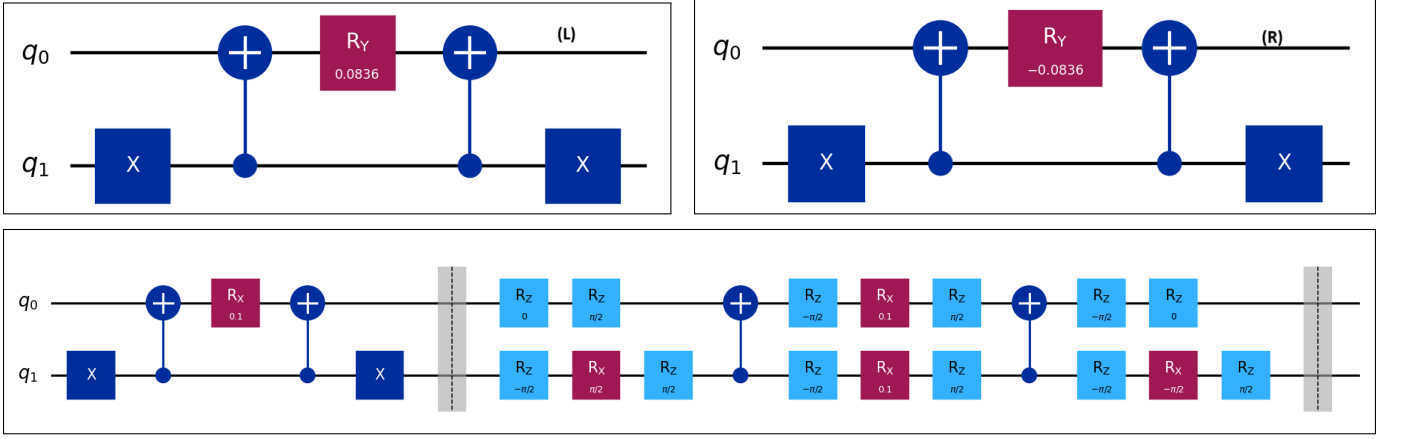


FIG. 2. Circuits implementing the $\Omega_Q \rightarrow \Omega_P \rightarrow \Omega_S$ sequence for L and R enantiomers, with the input state being $|00\rangle$. **Top row:** Panel(L) shows the quantum circuit for the Q-pulse applied to L enantiomers, while panel(R) shows the corresponding circuit for R enantiomers. The Q-pulse encodes the phase signature of L and R enantiomers through the rotational gate $R_y(\pm\theta_i)$ at each time step, with $\theta_i = \Omega_Q(t_i) \delta t$. **Bottom row:** (i) The P -pulse drives the $|00\rangle \leftrightarrow |11\rangle$ transition by encoding its amplitude $\Omega_P(t)$ in controlled $R_x(\theta_i)$ rotational gate, where $\theta_i = \Omega_P(t_i) \delta t$. (ii) The S -pulse, applied after P , encodes its amplitude via a sequence of R_z and R_x rotational gates. **Measurement:** Both qubits are measured in the computational basis, and the resulting bitstring frequencies yield the populations P_{00} , P_{01} , and P_{10} .

the state of the L is driven from initial state $|00\rangle$ to $|\Psi\rangle_L = \frac{1}{\sqrt{2}}(|00\rangle_L - |10\rangle_L)$ and ends up at $-|10\rangle_L$ as shown in the Fig. 4. The matrix form for $H_{PS}(t)$ reads as

$$H_{PS} = \frac{1}{2} \begin{pmatrix} 0 & \Omega_P e^{i\phi_P} & 0 \\ \Omega_P e^{-i\phi_P} & 0 & \Omega_S e^{i\phi_S} \\ 0 & \Omega_S e^{-i\phi_S} & 0 \end{pmatrix} \quad (11)$$

There are three instantaneous eigenstates with 0 and $\pm \frac{\Omega(t)}{2}$ eigenenergies respectively.

$$|\gamma_0\rangle = \cos \alpha_1 |00\rangle - \sin \alpha_1 |10\rangle \quad (12)$$

$$|\gamma_{\pm}\rangle = (e^{i(\phi_P + \phi_S)} \sin \alpha_1 |00\rangle \pm e^{i\phi_S} |11\rangle + \cos \alpha_1 |10\rangle) \quad (13)$$

The total Rabi frequency $\Omega(t) = \sqrt{\Omega_S^2(t) + \Omega_P^2(t)}$ represents how effective the coupling strength is when the transition is occurring between $|00\rangle \leftrightarrow |11\rangle$ and $|11\rangle \leftrightarrow |10\rangle$ and quantifies the energy splitting between the instantaneous eigenstates of the Hamiltonian. When the P - and S -pulses possess nearly identical magnitudes, $\Omega_S(t) \approx \Omega_P(t)$, the total Rabi frequency reduces to $\Omega(t) \approx \sqrt{2} \Omega_S$, which reflects the equal contribution of each pulse. Conversely, when $\Omega_S(t) \approx 0$, the total Rabi frequency reduces to the amplitude of the P -pulse, indicating that the transition $|00\rangle \leftrightarrow |11\rangle$ is dominated by the P -pulse. The mixing angle $\alpha_1 = \tan^{-1}(\frac{\Omega_P}{\Omega_S})$ defines the system's eigenstate composition over time, leading to chiral discrimination of enantiomers. Under the adiabatic condition ($\dot{\alpha}_1 \ll \Omega(t)$) [20, 29] where $\dot{\alpha}_1 = \frac{d}{dt} \left[\tan^{-1}(\frac{\Omega_P}{\Omega_S}) \right]$ represent

how fast the field strength is changing, ensure that the Hamiltonian changes slowly compared to the energy gap ($\Omega(t)$) between the eigenstate and eventually prevent the nonadiabatic coupling between the $|\gamma_0\rangle$ and $|\gamma_{\pm}\rangle$, which are separated by an energy difference of $\pm \frac{\Omega}{2}$. Conversely, if the field changes too abruptly, the time rate of change in α_1 becomes large, and the system may undergo unwanted transitions between eigenstates, including leakage from the dark state $|\gamma_0\rangle$ to the bright states $|\gamma_{\pm}\rangle$. Consequently, start populating the intermediate state ($|2\rangle$) rather than populating the target state, which is key for chiral discrimination between two enantiomers.

After preparing the superposition states for the two enantiomers, $|\Psi\rangle_L = \frac{1}{\sqrt{2}}(|00\rangle_L - |10\rangle_L)$ and $|\Psi\rangle_R = \frac{1}{\sqrt{2}}(|00\rangle_R + |10\rangle_R)$, we proceed by applying the P - and S -pulses, which are the same for both L and R. Utilizing fractional STIRAP [33, 34], we aim to achieve robust population transfer from initial state $|00\rangle$ to target $|10\rangle$ by adiabatically varying $\alpha_1(t)$ from 0 to $\pi/2$. Initially, when $\alpha_1(t) \approx 0$, the dark state $|\gamma_0(t \approx 0)\rangle = \cos \alpha_1 |00\rangle - \sin \alpha_1 |10\rangle \approx |00\rangle$ is perfectly aligned with the ground state. Later, at $\alpha_1(t) \approx \frac{\pi}{4}$, the driving fields satisfy $\Omega_S(t) \approx \Omega_P(t)$, and the instantaneous eigenstate becomes $|\gamma_0(t = t_{1/2})\rangle \approx \frac{1}{\sqrt{2}}(|00\rangle - |10\rangle)$, which corresponds to maximal coherence. At the final stage, when $\alpha_1(t) \approx \frac{\pi}{2}$, the driving fields satisfy $\Omega_S(t) \ll \Omega_P(t)$, and the dark state evolves into $|\gamma_0(t = t_{1/2})\rangle \approx -|10\rangle$, signifying the complete transfer of population to the target state. Under adiabatic evolution, the L enantiomer follows the instantaneous dark eigenstate $|\gamma_0(t)\rangle$ and ultimately evolves into the target state $|10\rangle$. In contrast, the R-enantiomer, being orthogonal to the dark state $|\gamma_0(t)\rangle$, evolves as a superposition of the bright states $|\gamma_{\pm}(t)\rangle$. However, when a state evolves under a time-dependent Hamiltonian $H_{PS}(t)$, it acquires an overall dynamic phase, $\Phi_{\text{dyn}}(t) = -\frac{1}{\hbar} \int E(t) dt$ with $E(t)$ denoting the instantaneous eigenvalue of the system during evolu-

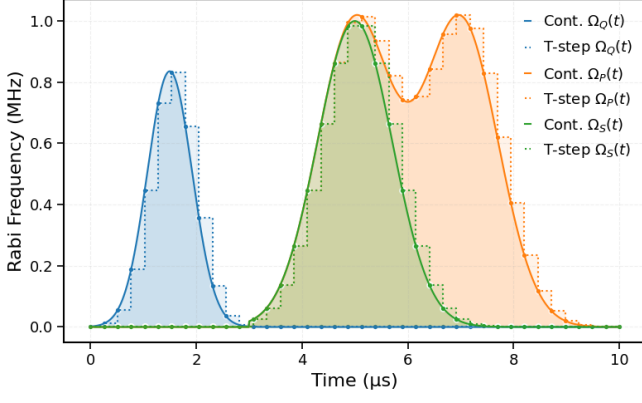


FIG. 3. Solid lines show the continuous Gaussian envelopes: $\Omega_Q(t)$ (blue), $\Omega_P(t)$ (orange), and $\Omega_S(t)$ (green). In contrast, dashed lines depict their Trotter decompositions into steps of fixed duration δt , preserving the integrated pulse area.

tion. For a given eigenstate $|\gamma_{\pm}(t)\rangle$ the instantaneous eigenvalue is $E_{\pm}(t) = \pm \frac{\Omega(t)}{2}$ thus the phase accumulated by $|\gamma_{\pm}(t)\rangle$ is: $\Phi_{\pm} = -\frac{1}{2} \int_{t=0}^{t=t_f} \Omega(t) dt$. Eventually, the final state becomes

$$|\Psi_R(t=t_f)\rangle = \frac{1}{\sqrt{2}} \left[e^{-\frac{i}{2} \int \Omega(t) dt} |\gamma_+(t=t_i)\rangle + e^{+\frac{i}{2} \int \Omega(t) dt} |\gamma_-(t=t_i)\rangle \right] \quad (14)$$

As the applied field $\Omega_S(t)$ and $\Omega_P(t)$ start at $t = t_i$ when $\alpha_1(t) \approx \frac{\pi}{4}$ the initial state of γ_{\pm} becomes $|\gamma_{\pm}(t=t_i)\rangle = \frac{1}{\sqrt{2}} (|00\rangle \pm |01\rangle + |10\rangle)$. Putting the value of $|\gamma_{\pm}(t=t_i)\rangle$ in Eq. (14)

$$|\Psi_R(t=t_f)\rangle = \frac{1}{2} \left[\cos\left(\frac{1}{2} \int \Omega(t) dt\right) (|00\rangle + |10\rangle) - i \sin\left(\frac{1}{2} \int \Omega(t) dt\right) |01\rangle \right] \quad (15)$$

At the final time $t = t_f$, the mixing angle approaches $\alpha_1(t) \approx \frac{\pi}{2}$, corresponding to the regime $\Omega_S(t) \ll \Omega_P(t)$. As a result, the state of the R enantiomer becomes

$$|\Psi_R(t_f)\rangle = \cos \rho |00\rangle + \sin \rho |11\rangle,$$

with $\rho = \frac{1}{2} \int \Omega(t) dt$. In this configuration, the dynamics dominantly couple the states $|00\rangle \leftrightarrow |11\rangle$, while the population of the R enantiomer in the state $|10\rangle$ vanishes due to destructive interference.

IV. RESULTS FOR STIMULATED RAMAN ADIABATIC PASSAGES (STIRAP)

We use Trotter decomposition to numerically evolve the states under the time-dependent Hamiltonian: $\hat{H}(t) = \hat{H}_Q(t) +$

$\hat{H}_{PS}(t)$. A first-order Trotter–Suzuki approximation is then applied, resulting in

$$e^{-i\hat{H}t} \approx \left(e^{-i\hat{H}\delta t} \right)^m \approx \left(e^{-i\{\hat{H}_Q + \hat{H}_{PS}\}\delta t} \right)^m \quad (16)$$

where $\delta t = \frac{t}{m}$ is the step size and m is the total number of steps. To generate the initial superposition through the $\Omega_Q(t)$ pulse, we first apply k number of Trotter steps ($U_Q^{(i)} = \prod_{i=1}^m e^{-iH_Q(t_i)\delta t}$). Following this initialization, the subsequent evolution is governed by $e^{-i\hat{H}_{PS}\delta t}$. Therefore, the overall Trotter decomposition can be expressed as

$$e^{-i\hat{H}t} \approx \left(e^{-i\hat{H}_Q\delta t} \right)^k \left(e^{-i\hat{H}_{PS}\delta t} \right)^{m-k} + O(\delta t^2) \quad (17)$$

Finally, we implemented $\Omega_Q(t)$, $\Omega_P(t)$ and $\Omega_S(t)$ pulses using the Trotter decomposition and divided the continuous Gaussian pulses into a discrete rectangular shape as shown in Fig. 3. The $\Omega_Q(t)$ pulse (blue dashed line) starts at $t = 0$ and ends at $t \approx 3 \mu s$. During this interval, the L and R enantiomers are driven from the initial state $|00\rangle$ to $|\Psi\rangle_L = \frac{1}{\sqrt{2}}(|00\rangle_L - |10\rangle_L)$ and $|\Psi\rangle_R = \frac{1}{\sqrt{2}}(|00\rangle_R + |10\rangle_R)$, respectively. The green continuous Gaussian shape represents the $\Omega_S(t)$ pulse, which drives the transition from the intermediate state $|11\rangle$ to the target state $|10\rangle$. We apply it before the $\Omega_P(t)$ (orange dashed line), which is responsible for $|00\rangle$ to $|11\rangle$ population transitions. The reason for applying $\Omega_S(t)$ first is intuitive; the dark state $|\gamma_0(t)\rangle$ is a superposition of $|00\rangle$ and $|10\rangle$ that decouples from $|11\rangle$ and is immune to the spontaneous emission of $|11\rangle$. Therefore, when the $\Omega_S(t)$ pulse is applied first, it couples $|11\rangle \leftrightarrow |10\rangle$, while the transition $|00\rangle \leftrightarrow |11\rangle$ remains off ($\Omega_P(t) = 0$). In this case, the mixing angle satisfies $\alpha_1(t) = 0$, and the system begins in $|00\rangle$, which coincides with the dark state. As $\Omega_P(t)$ starts to increase gradually, the mixing angle starts from $\alpha_1(t=0) \approx 0$ to reach an intermediate value of $\alpha_1(t_{1/2}) \approx \frac{\pi}{4}$ and ends up to $\alpha_1(t=t_f) \approx \frac{\pi}{2}$. As a result, when the applied field varies sufficiently slowly, the system remains in the dark state throughout the process, enabling population transfer from the initial state $|00\rangle$ to the target state $|10\rangle$ without populating the intermediate state $|11\rangle$. Fig. 3 illustrates that discretizing the Gaussian pulses into only 20 Trotter steps introduces a noticeable Trotter error. Increasing the resolution by employing a finer grid for the pulse discretization progressively reduces this error, $\epsilon(1/N)$. However, the computational cost of the simulation grows linearly as $O(N)$, where N is the number of Trotter steps.

As shown in Fig. 4(a), we apply the STIRAP scheme using exact diagonalization with QuTiP (green solid line), a statevector simulator (green dashed line), and finally, we benchmark the STIRAP protocol using two IBM quantum processors (yellow dotted line). In Fig. 4(a), we employ ibm_kingston, which exhibits results closely matching the QuTiP exact simulation, while Fig. 4(b) presents results from ibm_fez, where noticeable oscillations appear near the end, likely due to hardware

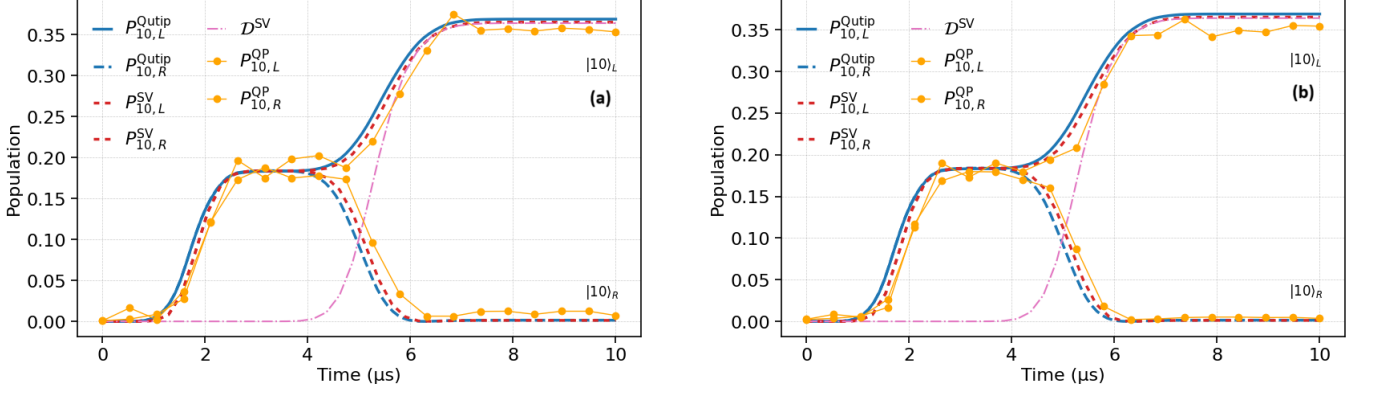


FIG. 4. Chiral discrimination of L and R enantiomers using the Stimulated Raman Adiabatic Passage (STIRAP) scheme. Exact diagonalization with QuTiP (blue solid), the statevector simulator (red dashed), and quantum processor experiments (yellow solid) are shown. Panels (a) and (b) show benchmarking of the exact diagonalization results with (ibm_kingston and ibm_fez) quantum processors.

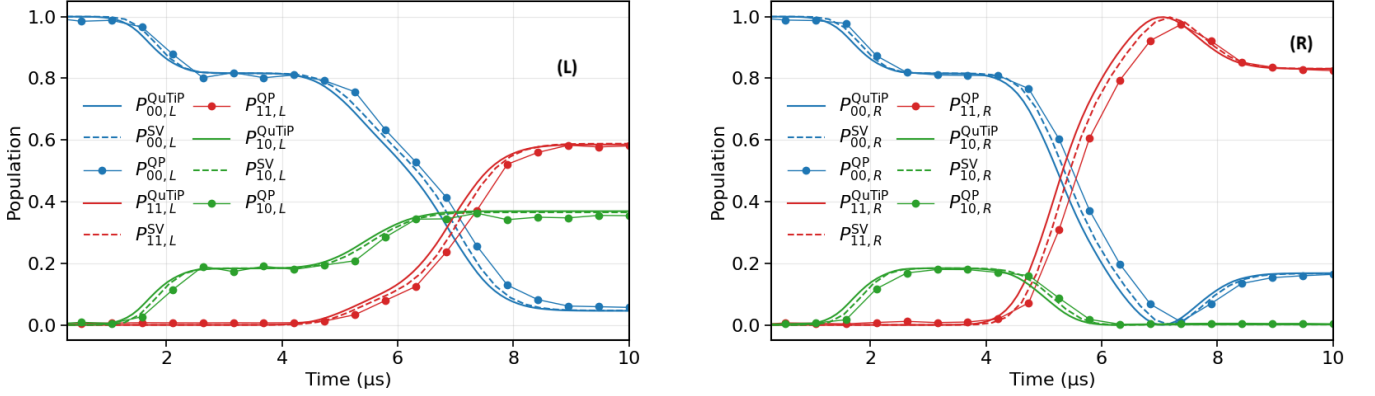


FIG. 5. Time evolution of L and R enantiomers under Stimulated Raman Adiabatic Passage (STIRAP) protocol for $|00\rangle$ (blue), $|11\rangle$ (red), and $|10\rangle$ (green) states, obtained from: (i) exact diagonalization using QuTiP ($P^{(\text{QuTiP})}$), (ii) statevector simulator of the discretized quantum circuit ($P^{(\text{SV})}$), and (iii) benchmarking of the exact diagonalization results with quantum processors ($P^{(\text{QP})}$).

noise and unwanted transitions arising from nonadiabatic effects. The circuit was executed on both quantum processors with 5,000 shots to obtain accurate output statistics. We used the IBM Quantum Runtime Sampler, which lacks built-in error mitigation. However, no correction or suppression techniques were applied, such as gate twirling or dynamical decoupling. Sec. V uses the same experimental conditions.

From Fig. 4(a) and Fig. 4(b), the results of the quantum computer closely match the QuTiP simulations, even for $t \approx 5 \mu\text{s}$. This agreement demonstrates that the system reliably evolves toward their target states once discrimination between the L and R enantiomers is achieved. The R enantiomer does not populate the state $|10\rangle$, as its evolution leads to a superposition of $|00\rangle$ and $|11\rangle$. Contrarily, the L molecule should be completely populated in state $|10\rangle$, but from the results, the probability of being in state $|10\rangle$ is less than 40%. The primary reason is the slow adiabatic evolution ($\dot{\alpha}_1 \ll \Omega$) to keep the L enantiomers in the dark state $|\gamma_0(t)\rangle$, but the rate of change of the pulses is higher ($\dot{\alpha}_1 \sim \Omega$); therefore, the system leaks into other states ($|\gamma_{\pm}\rangle$).

Another reason for the lower fidelity of L enantiomers is imperfect superposition created by Q -pulse, ideally the state $|00\rangle$ and $|10\rangle$ should have equal superposition. In Fig. 5 the green curve ($|10\rangle$) illustrates how the L and R enantiomers evolve toward their respective target states. Conversely, the red and blue curves represent the time dynamics of the $|00\rangle$ and $|11\rangle$ states respectively. However, the measured probability of $|00\rangle$ and $|10\rangle$ states is lower than the theoretically predicted value after the Q -pulse is applied.

In Fig. 7, we present bar charts showing the state probabilities for $|00\rangle$, $|11\rangle$, and $|10\rangle$. These are evaluated at the midpoint of the Q -pulse ($t = 0.61 \mu\text{s}$) and at its end ($t = 2.53 \mu\text{s}$). At $t = 2.53 \mu\text{s}$, the measured probabilities for $|00\rangle$ and $|10\rangle$ are 0.82 and 0.18, respectively, for both L and R enantiomers. Ideally, the final state should approach an equal superposition, $|\Psi\rangle_L = \frac{1}{\sqrt{2}}(|00\rangle_L - |10\rangle_L)$ and $|\Psi\rangle_R = \frac{1}{\sqrt{2}}(|00\rangle_R + |10\rangle_R)$, when the Q -pulse is fully applied.

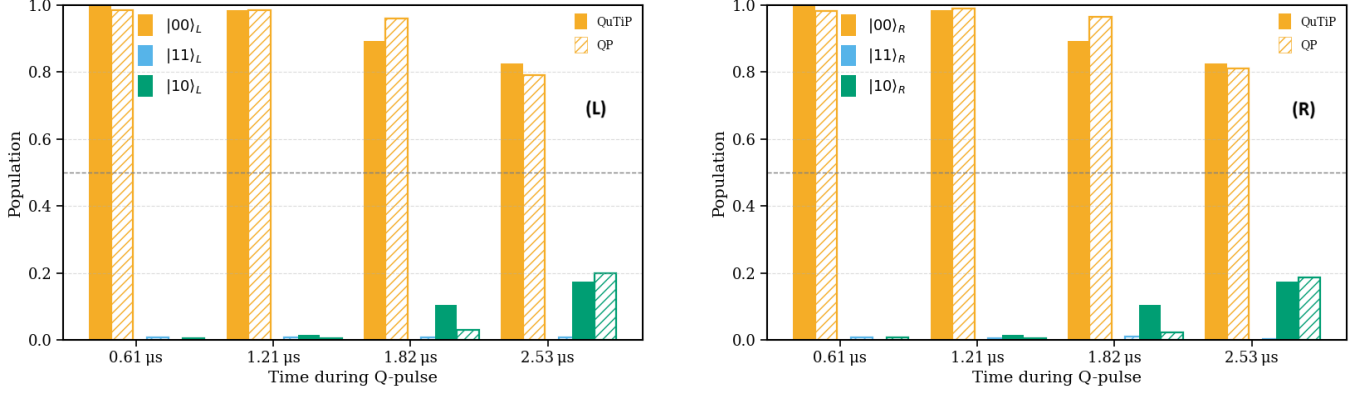


FIG. 6. State populations $|00\rangle$ (orange), $|11\rangle$ (blue), and $|10\rangle$ (green) at the midpoint ($t = 0.61 \mu s$) and end ($t = 2.53 \mu s$) of the $\Omega_Q(t)$ pulse, under Stimulated Raman Adiabatic Passage (STRIP) scheme. Bars with hatched fill represent results from the quantum processor, while solid bars show exact diagonalization using QuTiP, for both enantiomers.

V. SHORTCUTS TO ADIABATIC PASSAGE (STAP)

A. Mathematical formulation

Based on the given results, it is evident that STIRAP is not following the adiabatic evolution ($\dot{\alpha}_1 \ll \Omega$) completely which makes it less efficient to discriminate L and R enantiomers. Therefore we need to engineer the pulse shape and instantaneous eigenstate to get a higher population of L in state $|10\rangle$. To address this Limitation: Shortcuts-to-Adiabatic Passage (STAP) is a powerful technique [28], in which we tailored controlled pulses that enable state transfer into the target state in a short interval of time by suppressing unwanted transitions.

Consider the same three-level system ($|00\rangle$, $|11\rangle$, and $|10\rangle$) interacting with a time-dependent controlled field $\Omega_P(t)$ and $\Omega_S(t)$. The Hamiltonian in the Rotating Wave Approximation (RWA) frame becomes

$$H_{PS}(t) = \Omega_P(t)|00\rangle\langle 11| + \Omega_S(t)|11\rangle\langle 10| + \text{h.c.} \quad (18)$$

The three instantaneous eigenvalues 0 and $\pm \frac{\Omega(t)}{2}$ corresponding to eigenstates are

$$|\gamma_0\rangle = \cos \alpha_1 |00\rangle - \sin \alpha_1 |10\rangle \quad (19)$$

$$|\gamma_{\pm}\rangle = (e^{i(\phi_P + \phi_S)} \sin \alpha_1 |00\rangle \pm e^{i\phi_S} |11\rangle + \cos \alpha_1 |10\rangle) \quad (20)$$

The transformation of $H_{PS}(t)$ into adiabatic frame gives two main results: (i) instantaneous eigenstate ($|\gamma_{\pm,0}(t)\rangle$) transforms into time independent states and non-adiabatic coupling terms ($\dot{\alpha}_1(t)$) appear explicitly in the transformed Hamiltonian $H_I(t)$. The detailed derivation is in the Appendix C. The adiabatic transformation is given as

$$U_0(t) = \sum_{n=0,\pm} |\gamma_n\rangle\langle \gamma_n(t)| \quad (21)$$

The Hamiltonian in the adiabatic frame takes the form

$$H_I(t) = U_0(t)H_{PS}(t)U_0^\dagger(t) - iU_0(t)\dot{U}_0^\dagger(t) \quad (22)$$

Putting the value of $U_0(t)$ in Eq. (22)

$$H_I(t) = \Omega(t) \left[|\gamma_+\rangle\langle \gamma_+| - |\gamma_-\rangle\langle \gamma_-| \right] + \frac{\dot{\alpha}_1(t)}{\sqrt{2}} \left[|\gamma_+\rangle\langle \gamma_0| + |\gamma_-\rangle\langle \gamma_0| \right] + \text{h.c.} \quad (23)$$

The nonadiabatic coupling terms, which are now directly visible in the adiabatic frame, are responsible for the leakage of dark state $|\gamma_0(t)\rangle$ into $|\gamma_{\pm}(t)\rangle$. Now the goal of STAP is to cancel these nonadiabatic coupling terms by introducing a controlled auxiliary field $\Omega'_P(t)$ and $\Omega'_S(t)$, and this was not possible without transforming the Hamiltonian $H_{PS}(t)$ into the adiabatic frame. Designing the auxiliary pulses is difficult because the unwanted coupling is hidden in the lab frame.

Combining the controlled auxiliary field with the STIRAP protocol speeds up the population from the initial state to the target state. In this case, the Hamiltonian takes the form

$$H'(t) = [\Omega_P(t) + \Omega'_P(t)]|00\rangle\langle 11| + [\Omega_S(t) + \Omega'_S(t)]|11\rangle\langle 10| + \text{h.c.} \quad (24)$$

where $\Omega'_P(t)$ and $\Omega'_S(t)$ are the auxiliary pulses combined with original pulses $\Omega_P(t)$ and $\Omega_S(t)$ respectively. For $|\varphi_0(t)\rangle$ to act as an evolution state for modifying Hamiltonian $H'(t)$, it must guarantee the same final state $|\gamma_0(t)\rangle$. Therefore, we can choose the following dressed state, which ensures the same final state

$$|\varphi_0(t)\rangle = \cos \theta_2(t) \left[\cos \alpha_1(t) |00\rangle + e^{i\phi} \sin \alpha_2(t) |11\rangle + \sin \alpha_1(t) |10\rangle \right] \quad (25)$$

The following boundary conditions will ensure the same final state $|\gamma_0(t)\rangle$

$$\begin{cases} \alpha_1(t=0) = \frac{\pi}{4}, \\ \alpha_1(t=t_f) = \frac{\pi}{2}, \\ \alpha_2(t=0) = \alpha_2(t=t_f) = 0 \end{cases} \quad (26)$$

The other dressed states $|\varphi_{\pm}(t)\rangle$ are constructed in such a way that they should be orthogonal to $|\varphi_0(t)\rangle$ under the modified Hamiltonian $H'(t)$. Therefore, to form a complete set of orthogonal states, the non-adiabatic state $|\varphi_{\pm}(t)\rangle$ must satisfy the following conditions: (i) $\langle\varphi_i(t)|\varphi_j(t)\rangle = \delta_{ij}$ where $i, j = \pm, 0$ (ii) $\sum_{n=0,\pm} |\varphi_n\rangle\langle\varphi_n| = 1$ [35]. Then the chosen dressed states become

$$\begin{aligned} |\varphi_{\pm}(t)\rangle = \frac{1}{\sqrt{2}} \Big\{ & \left[\sin \alpha_2(t) \mp \sin \alpha_2(t) \cos \alpha_1(t) \right] |00\rangle \\ & \mp \cos \alpha_2(t) |11\rangle \\ & - \left[\cos \alpha_1(t) \pm i \sin \alpha_2(t) \sin \alpha_1(t) \right] |10\rangle \Big\} \end{aligned} \quad (27)$$

The auxiliary controlled pulses are designed to guide $|\varphi_0(t)\rangle$ along the chosen path by decoupling it from the non-adiabatic states $|\varphi_{\pm}(t)\rangle$. Following the same approach we used to transform Hamiltonian $H_{PS}(t)$ into the adiabatic frame, applying $U_1(t) = \sum_{n=0,\pm} |\varphi_n\rangle\langle\varphi_n|$ to the Hamiltonian given in Eq. (32).

The Hamiltonian in the adiabatic frame takes the form

$$H'_{AD}(t) = U_1(t)H'(t)U_1^\dagger(t) - iU_1(t)\dot{U}_1^\dagger(t) \quad (28)$$

Both terms $\{U_1(t)H'(t)U_1^\dagger(t), iU_1(t)\dot{U}_1^\dagger(t)\}$ are explicitly calculated in Appendix D, and the final Hamiltonian becomes

$$\begin{aligned} H'_{AD}(t) = Y(t) & \left[|\varphi_+\rangle\langle\varphi_+| - |\varphi_-\rangle\langle\varphi_-| \right] \\ & + \left[\lambda_+(t) |\varphi_+(t)\rangle\langle\varphi_0(t)| + \lambda_-(t) |\varphi_-(t)\rangle\langle\varphi_0(t)| + \text{h.c.} \right] \end{aligned} \quad (29)$$

With three parameters:

$$\begin{aligned} Y(t) = & \left[\Omega'_S(t) \cos \alpha_1(t) - \Omega'_P(t) \sin \alpha_1(t) \right. \\ & \left. + \Omega \cos 2\alpha_1(t) \right] \cos \alpha_2(t) \end{aligned}$$

$$\begin{aligned} \lambda_{\pm}(t) = i & \left[\dot{\alpha}_1(t) \cos \alpha_2(t) - \sin \alpha_2(t) \left(\Omega'_S(t) \cos \alpha_1(t) \right. \right. \\ & \left. \left. - \Omega'_P(t) \sin \alpha_1(t) + \Omega \cos 2\alpha_1(t) \right) \right] \\ & \mp \left[\Omega'_P(t) \cos \alpha_1(t) - \Omega'_S(t) \sin \alpha_1(t) \right. \\ & \left. + \Omega \sin 2\alpha_1(t) + \dot{\alpha}_2(t) \right] \end{aligned}$$

It is evident that $\lambda_{\pm}(t)$ gives information about the coupling strength between $|\varphi_0\rangle\langle\varphi_0(t)|$ and $|\varphi_{\pm}\rangle\langle\varphi_{\pm}(t)|$. To guarantee that the system only follows $|\varphi_0(t)\rangle$, the auxiliary controlled pulses $\Omega'_P(t)$ and $\Omega'_S(t)$ are engineered in such a way that the transition amplitude $\lambda_{\pm}(t) = 0$.

For $\lambda_{\pm}(t) = 0$ and solving both equations for $\Omega'_P(t)$ and $\Omega'_S(t)$ gives

$$\begin{aligned} \Omega'_P(t) = & -\sin \alpha_1(t) \left[\dot{\alpha}_1(t) \cot \alpha_2(t) + \Omega(t) \right] \\ & - \dot{\alpha}_2(t) \cos \alpha_1(t) \end{aligned} \quad (30)$$

$$\begin{aligned} \Omega'_S(t) = & \cos \alpha_1(t) \left[\dot{\alpha}_1(t) \cot \alpha_2(t) - \Omega(t) \right] \\ & - \dot{\alpha}_2(t) \sin \alpha_1(t) \end{aligned} \quad (31)$$

Since $\Omega_S(t) = \Omega(t) \cos \alpha_1(t)$ and $\Omega_P(t) = \Omega(t) \sin \alpha_1(t)$

$$\begin{aligned} \Omega_P(t) + \Omega'_P(t) = & -\dot{\alpha}_1(t) \sin \alpha_1(t) \cot \alpha_2(t) \\ & - \dot{\alpha}_2(t) \cos \alpha_1(t) \end{aligned} \quad (32)$$

and

$$\Omega_S(t) + \Omega'_S(t) = \dot{\alpha}_1(t) \cos \alpha_1(t) \cot \alpha_2(t) - \dot{\alpha}_2(t) \sin \alpha_1(t) \quad (33)$$

By employing the modified Rabi frequency given in the Eq. (32) and (33), the system follows the three level multi-photon path $\{|\varphi_0(t)\rangle, |\varphi_{\pm}(t)\rangle\}$. Once the superposition $|\Psi\rangle_L = \frac{1}{\sqrt{2}}(|00\rangle_L - |10\rangle_L)$ and $|\Psi\rangle_R = \frac{1}{\sqrt{2}}(|00\rangle_R + |10\rangle_R)$ is created by applying $\Omega_Q(t)$ pulse, the modified Rabi frequency will drive the L and R molecules to their respective final states:

$$|\Psi(t=t_f)\rangle_L = -|10\rangle_L$$

$$|\Psi_R(t=t_f)\rangle = \cos \rho^c |00\rangle + \sin \rho^c |11\rangle$$

Where $\rho^c = \frac{1}{2}(\int Y(t)dt)$ over the time interval $t_0 \rightarrow t_f$.

B. Real Molecule: 1,2-propanediol

For a general asymmetric molecule [36], the rotational energy levels are governed by a rigid rotor Hamiltonian

$$\hat{H}_{rot} = A\hat{J}_A^2 + B\hat{J}_B^2 + C\hat{J}_C^2 \quad (34)$$

where $A = \frac{\hbar^2}{2I_A}$, $B = \frac{\hbar^2}{2I_B}$, $C = \frac{\hbar^2}{2I_C}$ and $I_A \neq I_B \neq I_C$

The angular momentum operators \hat{J}_A , \hat{J}_B , and \hat{J}_C account for the principal axis which serves as a good quantum number, but asymmetrical molecules do not conserve the projection quantum number K . In symmetric top molecules, K is the

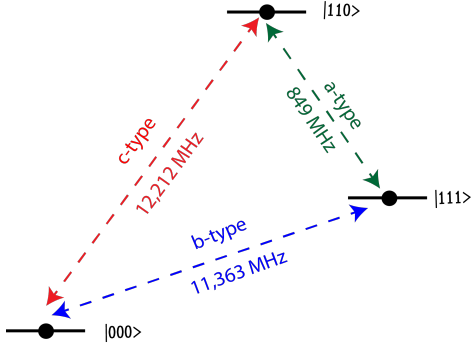


FIG. 7. Allowed transition pulses $\Omega_Q(t)$, $\Omega_P(t)$, and $\Omega_S(t)$ in the chiral molecule 1,2-propanediol (propylene glycol, $C_3H_8O_2$).

quantum number associated with the projection of total angular momentum \vec{J} onto a molecule-fixed axis. If the molecule-fixed axis is the z-axis, then \hat{J}_z commutes with the Hamiltonian, conserving the projection quantum number K .

$$[\hat{H}, \hat{J}_z] = 0 \Rightarrow K = \text{constant}$$

As for asymmetric top molecules, $I_A \neq I_B \neq I_C$, none of the components of \hat{J}_A , \hat{J}_B , and \hat{J}_C commute with the Hamiltonian \hat{H}_{rot}

$$[\hat{H}_{rot}, \hat{J}_A] \neq 0, \quad [\hat{H}_{rot}, \hat{J}_B] \neq 0, \quad [\hat{H}_{rot}, \hat{J}_C] \neq 0$$

Therefore, no projection of the total angular momentum \vec{J} along the molecule-fixed axis is conserved. To label the rotational energy level for an asymmetric top we still use $|J_{K_a, K_c}\rangle$ where K_a, K_c are projections of \vec{J} along the principal axes a and c . We consider 1,2-propanediol (propylene glycol, $C_3H_8O_2$) as an asymmetric molecule to verify this scheme using a quantum computer and discuss its future implications.

In the present scheme, we consider a closed-loop configuration $|1\rangle \leftrightarrow |2\rangle \leftrightarrow |3\rangle \leftrightarrow |1\rangle$. The rotational energy level $|J_{K_a, K_c}\rangle$ is encoded in a two-qubit representation, defined by the computational basis states $\{|00\rangle, |01\rangle, |10\rangle, |11\rangle\}$. From the experimental microwave spectroscopy [37], the rotational constants for a conformer of 1,2-Propanediol ($C_3H_8O_2$) are: $A = 5872.06 \text{ MHz}$, $B = 3640.11 \text{ MHz}$ and $C = 2790.97 \text{ MHz}$. The electric dipole moment $\vec{\mu}$ has nonzero projections along all three principal axes: $\mu_a = 1.201 \text{ D}$, $\mu_b = 1.916 \text{ D}$, and $\mu_c = 0.365 \text{ D}$. These components determine the selection rules for a -, b -, and c -type transitions, respectively. For a closed-loop system, the mapping of qubit states to rotational energy states is

$$\begin{aligned} |00\rangle : & \quad J = 0, K_a = 0, K_c = 0, \\ |11\rangle : & \quad J = 1, K_a = 1, K_c = 1, \\ |10\rangle : & \quad J = 1, K_a = 1, K_c = 0. \end{aligned} \quad (35)$$

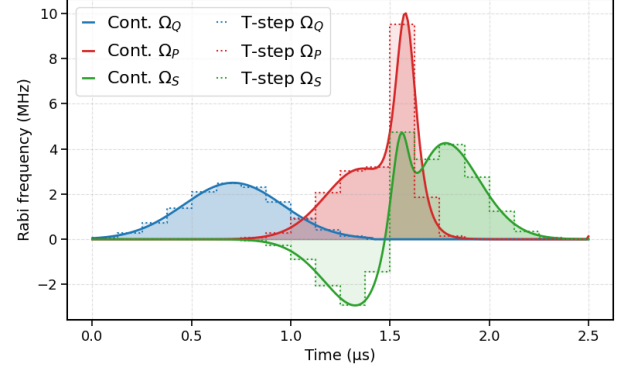


FIG. 8. Continuous Gaussian envelopes after adding counter-diabatic pulses: $\Omega_Q(t)$ (blue), $\Omega_P(t) + \Omega'_P(t)$ (red), $\Omega_S(t) + \Omega'_S(t)$ (green). The dashed line shows the Trotterized pulses with step size δt , preserving the total pulse area.

The transition frequencies [38], which correspond to the energy differences between the respective states (and hence the microwave frequencies required to drive the transitions), are given by

$$\begin{aligned} \omega_{00,11} &= \frac{E_{|11\rangle} - E_{|00\rangle}}{\hbar} = 11363 \text{ MHz}, \\ \omega_{00,10} &= \frac{E_{|10\rangle} - E_{|00\rangle}}{\hbar} = 12212 \text{ MHz}, \\ \omega_{11,10} &= \frac{E_{|10\rangle} - E_{|11\rangle}}{\hbar} = 849 \text{ MHz}. \end{aligned} \quad (36)$$

For the 1,2-propanediol closed-loop system, the c -type transition is driven by the $\Omega_Q(t)$ pulse between $|00\rangle \leftrightarrow |10\rangle$ with frequency $\omega_{00,10} = 12212 \text{ MHz}$. Owing to the opposite signs of this transition in the two enantiomers, it becomes the key mechanism for discrimination. The a -type transition is driven by $\Omega_S(t)$ pulse between $|11\rangle \leftrightarrow |10\rangle$ with frequency $\omega_{11,10} = 849 \text{ MHz}$ and b -type transition is driven resonantly by $\Omega_P(t)$ between $|00\rangle \leftrightarrow |11\rangle$ with frequency $\omega_{00,11} = 11363 \text{ MHz}$. The Rabi frequency $\Omega_j(t)$ for each transition ($j = P, Q, S$) is determined by the interaction between the transition dipole moment μ_j and the applied electric field ϵ_j

$$\Omega_j(t) = \frac{\vec{\mu}_j \cdot \vec{\epsilon}_j}{\hbar} \quad (37)$$

The field strengths of 0–2 V/cm produce the following Rabi frequencies: $\Omega_P(t) \approx 10\text{--}12 \text{ MHz}$ for the $|00\rangle \leftrightarrow |11\rangle$ transition, $\Omega_S(t) \approx 5\text{--}8 \text{ MHz}$ for the $|11\rangle \leftrightarrow |10\rangle$ transition, and $\Omega_Q(t) \approx 2.5\text{--}3 \text{ MHz}$ for the $|00\rangle \leftrightarrow |10\rangle$ transition, as shown in Fig. 7. These frequencies ensure the phase stability which is critical for enantiomer discrimination and coherent population transfer without higher power distortions. Most importantly, the field strength of $0 \sim 2 \text{ V/cm}$ is experimentally accessible and yields MHz scale $\Omega_j(t)$, which satisfies the Rotating-Wave approximation ($\Omega_j(t) \ll \omega_j$).

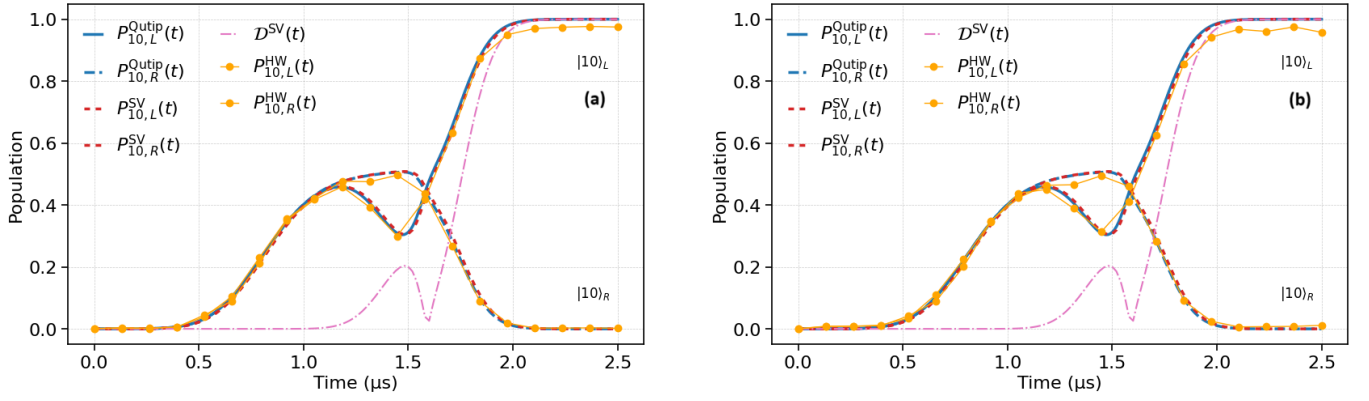


FIG. 9. Chiral discrimination of L and R enantiomers for 1,2-Propanediol ($\text{C}_3\text{H}_8\text{O}_2$), using the Shortcuts-to-Adiabaticity Passage (STAP) scheme. Exact diagonalization with QuTiP (blue solid), the statevector simulator (red dashed), and quantum processor experiments (yellow solid) are shown. Panels (a) and (b) show benchmarking of the exact diagonalization results with (ibm_kingston and ibm_fez) quantum processors.

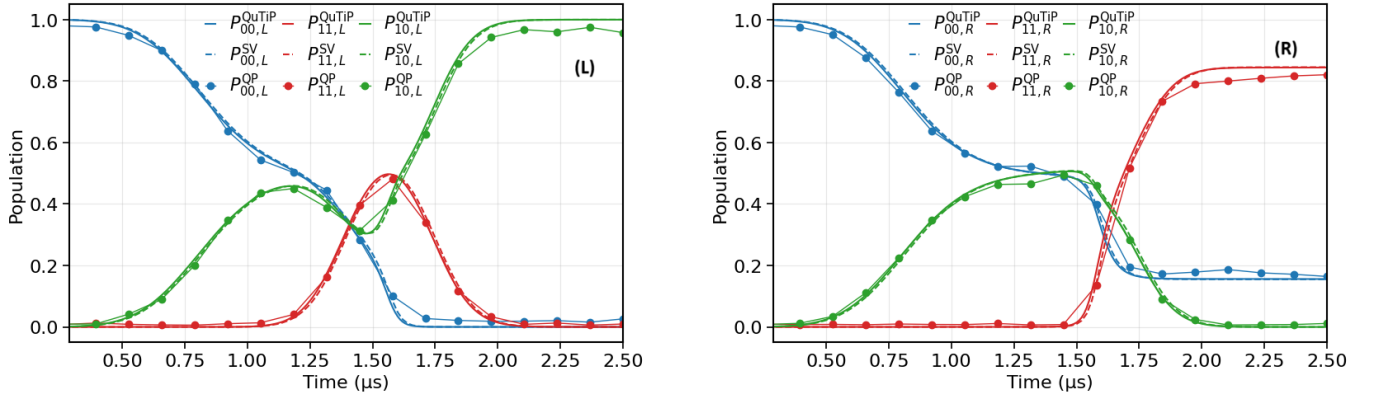


FIG. 10. Time evolution of L and R enantiomers under Shortcuts-to-Adiabaticity Passage (STAP) protocol for $|00\rangle$ (blue), $|11\rangle$ (red), and $|10\rangle$ (green) states: (i) exact diagonalization using QuTiP (P^{QuTiP}), (ii) quantum circuit simulation performed with the statevector simulator (P^{SV}), and (iii) benchmarking of the exact diagonalization results with quantum processors (P^{QP}).

Similarly, for STAP, we used Trotter Decomposition to divide the continuous Gaussian pulses into discrete rectangular shapes as shown in Fig. 8. The $\Omega_Q(t)$ pulse begins at $t = 0$ and peaks at $t \approx 1.5 \mu\text{s}$, driving L and R enantiomers from the initial state $|00\rangle$ to $|\Psi\rangle_L = \frac{1}{\sqrt{2}}(|00\rangle_L - |10\rangle_L)$ and $|\Psi\rangle_R = \frac{1}{\sqrt{2}}(|00\rangle_R + |10\rangle_R)$, respectively. Two parameters, $\alpha_1(t)$ and $\alpha_2(t)$, mainly control the time and shape of the pulses in STAP. In particular, $\alpha_1(t)$ controls the superposition between states $|00\rangle$ and $|10\rangle$, analogous to the STIRAP mixing angle. Meanwhile, $\alpha_2(t)$ regulates the intermediate-state population $|11\rangle$, functioning as a counter-adiabatic controller. In STIRAP, the adiabatic condition $|\frac{\dot{\theta}}{\Omega(t)}| \ll 1$ requires slowly varying pulses (long interaction times T). However, in the STAP protocol, the pulse shapes adapt dynamically to the time derivatives of $\alpha_1(t)$ and $\alpha_2(t)$.

For instance, near the intermediate state ($\alpha_1 \approx \frac{\pi}{4}$) of the STIRAP pulse sequence, $\alpha_1(t)$ varies most rapidly, making the system particularly susceptible to nonadiabatic transitions. At

this point, the scheme applies a counter-adiabatic correction when $\dot{\alpha}_1(t)$ is large. Consequently, rapid variations in $\alpha_1(t)$ are compensated by an appropriately tuned counter-adiabatic correction $\alpha_2(t)$, which removes the adiabatic constraint and enables short pulse durations ($T \approx 10 \mu\text{s}$ to $T = 2.5 \mu\text{s}$), as shown in Fig. 9. Following the boundary conditions at time t_i and t_f , we require $\alpha_2(t_i) = \alpha_2(t_f) = 0$, and the engineered eigenstates must match the original adiabatic states. We can ensure these boundary conditions with a Gaussian function: $\alpha_2(t) = \alpha_m(t)e^{-[(t-t_i)-(t_f-t_i)/2]^2/T_{a_2}^2}$ where $T_{a_2} = (t_f - t_i)/6$.

In Fig. 9, we show the time evolution of the target state $|10\rangle$ under the Shortcut-to-Adiabatic Passage (STAP) scheme. The blue solid line corresponds to the QuTiP simulation, representing the ideal population transfer. For the L enantiomer, the population monotonically increases to $P_{L \rightarrow |10\rangle} = |\langle \Psi_L | 10 \rangle|^2 \approx 1.0$, demonstrating perfect transfer under STAP-accelerated adiabatic conditions. The red dashed line shows the statevector simulator results, which deviate slightly from the QuTiP curve due to finite Trotterization and pulse-discretization approximations. Nevertheless, the agree-

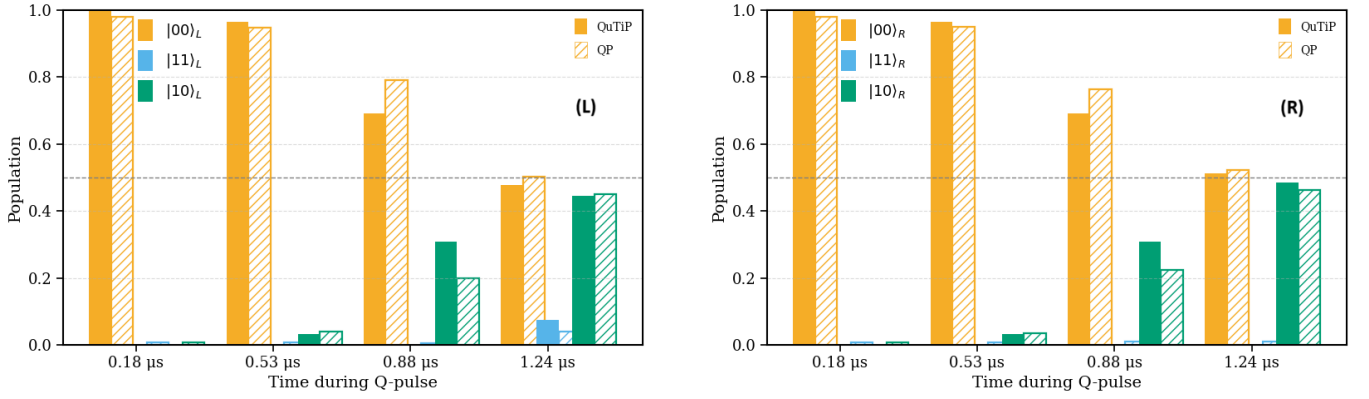


FIG. 11. State populations $|00\rangle$ (orange), $|11\rangle$ (blue), and $|10\rangle$ (green) at the midpoint ($t = 0.61 \mu s$) and end ($t = 2.53 \mu s$) of the $\Omega_Q(t)$ pulse, under Shortcuts to Adiabatic Passage (STAP) scheme. Bars with hatched fill represent results from the quantum processor, while solid bars show exact diagonalization using QuTiP, for both enantiomers.

ment validates the protocol’s robustness to Trotter error. The yellow dotted line represents the experimental benchmark obtained from two IBM quantum processors. As illustrated in Fig. 9(a), `ibm_kingston` processor achieves greater accuracy than `ibm_fez` Fig. 9(b), primarily because of its longer coherence times. Despite hardware limitations, the STAP protocol maintains a discrimination fidelity of $D(t) \approx 0.7\text{--}0.8$, underscoring its robustness and potential applicability on current quantum hardware.

As shown in Fig. 4, STAP achieves enantio-discrimination within $2.5 \mu s$, a five-fold speedup over STIRAP ($10 \mu s$), by employing analytically designed counteradiabatic pulses ($\Omega'_P(t), \Omega'_S(t)$) that guarantee adiabatic-like evolution. Such improvements in speed and precision are particularly valuable for the quantum simulation of large degenerate chiral molecules, where both temporal efficiency and high fidelity are essential. By significantly reducing the overall process time, the STAP scheme allows the quantum processor to execute simulations more accurately, enabling up to five times more Trotter steps within the same physical coherence window.

Fig. 10(L) and Fig. 10(R) present the time evolution of $|00\rangle$, $|11\rangle$, and $|10\rangle$ states for L and R enantiomers, demonstrating how the counter-adiabatic fields ($\Omega'_P(t)$ and $\Omega'_S(t)$) guide the population transfer from the initial state. The green curve ($|10\rangle$) highlights the successful transfer of the L and R enantiomers to the target state. In contrast, the red ($|00\rangle$) and blue ($|11\rangle$) curves trace the depletion of the initial populations, demonstrating how the STAP protocol redistributes population across the three levels. From Fig. 10, it is clear that, when a $\Omega_Q(t)$ pulse is applied initially to create the superposition, the $|00\rangle$ and $|10\rangle$ achieve a higher population in their target states for both L and R, which shows that the STAP actively suppressed nonadiabatic transitions by shortening the time process. In Fig. 11, the $|00\rangle$ and $|10\rangle$ states are shown as orange and green bars, while the blue bars correspond to $|11\rangle$ state. Bars with hatched fill represent results from the quantum processor, while solid bars show exact diagonalization using QuTiP, for both enantiomers. Remarkably, STAP produces

nearly ideal superpositions, $|\Psi_L\rangle = \frac{1}{\sqrt{2}}(|00\rangle_L - |10\rangle_L)$ and $|\Psi_R\rangle = \frac{1}{\sqrt{2}}(|00\rangle_R + |10\rangle_R)$, since the counter-adiabatic fields ($\Omega'_P(t), \Omega'_S(t)$) act early to suppress unwanted couplings and stabilize the dressed-state pathway. At $t = 2.53 \mu s$, once the $\Omega_Q(t)$ pulse is fully applied, STIRAP leaves the system with populations of 0.82 in $|00\rangle$ and 0.18 in $|10\rangle$ for both enantiomers. By contrast, STAP achieves the desired superposition much faster, yielding nearly equal probabilities of 0.52 and 0.48 at $t = 1.24 \mu s$.

VI. CONCLUSION

We have demonstrated a chiral discrimination scheme for the real molecule 1,2-propanediol using Stimulated Raman Adiabatic Passage (STIRAP), mapped onto a two-qubit quantum circuit, and experimentally benchmarked on IBM quantum processors. Under adiabatic conditions, the STIRAP protocol is inherently slow, allowing unwanted transitions that cause population leakage into intermediate states. As a result, it fails to efficiently transfer the population into the target states, making it unsuitable for experimental chiral discrimination. In contrast, implementing the Shortcuts-to-Adiabatic Passage (STAP) protocols markedly reduces evolution time and achieves higher-fidelity population transfer, resulting in clear separation of L and R enantiomers. These results establish a foundation for employing gate-based quantum computing to study and control molecular chirality, paving the way for investigations of more complex systems with degenerate energy states and developing quantum algorithms to probe enantiomer-specific interactions [5]. Beyond demonstrating chiral discrimination via STAP on gate-based platforms, a promising avenue is using quantum circuits to actively control molecular reaction pathways and unravel the complexity of chemical quantum dynamics [39–41].

The goal of simulating chiral discrimination on a gate-based quantum processor is not to test computational speed, but to examine whether the enantiomer-selective physics of

the three-level system survives when continuous control is replaced by a finite sequence of native gates under realistic noise. Our circuit mapping preserves the dark state structure and relative phases while discretizing the pulses, and hardware experiments show that even a modest number of Trotter slices can generate the expected Left/Right contrast, demonstrating that the discriminator is inherently robust in a digital setting. Running the protocol on an actual quantum processor, rather than a simulator, reveals how the signal withstands real noise and identifies the imperfections such as amplitude miscalibration or dephasing that most strongly affect performance. This provides a realistic estimate of the gates, qubits, and measurements required for success. Beyond confirming

the theory, these results show that our method for chiral discrimination remains effective under real-world noise and operates efficiently within the resource limits of current quantum hardware, thereby bridging a theoretical concept to a scalable quantum application.

VII. ACKNOWLEDGMENTS

The authors would like to acknowledge the financial support from the Quantum Science Center, a National Quantum Information Science Research Center of the U.S. Department of Energy (DOE).

-
- [1] B. Chu, *Laser light scattering: basic principles and practice* (Courier Corporation, 2007).
 - [2] R. Loudon, *The quantum theory of light* (OUP Oxford, 2000).
 - [3] X.-G. Wen, *Quantum field theory of many-body systems: From the origin of sound to an origin of light and electrons* (Oxford university press, 2004).
 - [4] P. Gibbon, *Short pulse laser interactions with matter: an introduction* (World Scientific, 2005).
 - [5] C. Brif, R. Chakrabarti, and H. Rabitz, *New Journal of Physics* **12**, 075008 (2010).
 - [6] B. L. Feringa and R. A. Van Delden, *Angewandte Chemie International Edition* **38**, 3418 (1999).
 - [7] W. A. Bonner, *Origins of Life and Evolution of the Biosphere* **21**, 59 (1991).
 - [8] J. E. Hein and D. G. Blackmond, *Accounts of chemical research* **45**, 2045 (2012).
 - [9] E. Yashima, N. Ousaka, D. Taura, K. Shimomura, T. Ikai, and K. Maeda, *Chemical reviews* **116**, 13752 (2016).
 - [10] M. Liu, L. Zhang, and T. Wang, *Chemical reviews* **115**, 7304 (2015).
 - [11] E. Herbst and E. F. Van Dishoeck, *Annual Review of Astronomy and Astrophysics* **47**, 427 (2009).
 - [12] S. M. Klausen and J. Parle, *Journal of Southern African Studies* **41**, 735 (2015).
 - [13] N. M. Maier, P. Franco, and W. Lindner, *Journal of Chromatography A* **906**, 3 (2001).
 - [14] L. A. Nafie, *Annual Review of Physical Chemistry* **48**, 357 (1997).
 - [15] Y. He, B. Wang, R. K. Dukor, and L. A. Nafie, *Applied spectroscopy* **65**, 699 (2011).
 - [16] B. P. Bloom, Y. Paltiel, R. Naaman, and D. H. Waldeck, *Chemical Reviews* **124**, 1950 (2024).
 - [17] R. Naaman, Y. Paltiel, and D. H. Waldeck, *Accounts of Chemical Research* **53**, 2659 (2020).
 - [18] G. Herzberg, *Molecular Spectra and Molecular Structure: Infrared and Raman Spectra of Polyatomic Molecules* (Van Nostrand Reinhold Company, New York, 1945).
 - [19] B. W. Shore, *The Theory of Coherent Atomic Excitation: Simple Atoms and Fields*, Vol. 1 (Wiley, New York, 1990).
 - [20] K. Bergmann, H. Theuer, and B. Shore, *Reviews of Modern Physics* **70**, 1003 (1998).
 - [21] N. Vitanov, M. Fleischhauer, B. Shore, and K. Bergmann, in *Advances in atomic, molecular, and optical physics*, Vol. 46 (Elsevier, 2001) pp. 55–190.
 - [22] N. V. Vitanov, A. A. Rangelov, B. W. Shore, and K. Bergmann, *Reviews of Modern Physics* **89**, 015006 (2017).
 - [23] Y. Li and C. Bruder, *Physical Review A—Atomic, Molecular, and Optical Physics* **77**, 015403 (2008).
 - [24] P. Král and M. Shapiro, *Physical Review Letters* **87**, 183002 (2001).
 - [25] D. Guéry-Odelin, A. Ruschhaupt, A. Kiely, E. Torrontegui, S. Martínez-Garaot, and J. G. Muga, *Reviews of Modern Physics* **91**, 045001 (2019).
 - [26] E. Torrontegui, S. Ibáñez, S. Martínez-Garaot, M. Modugno, A. del Campo, D. Guéry-Odelin, A. Ruschhaupt, X. Chen, and J. G. Muga, in *Advances in atomic, molecular, and optical physics*, Vol. 62 (Elsevier, 2013) pp. 117–169.
 - [27] X. Chen, I. Lizuain, A. Ruschhaupt, D. Guéry-Odelin, and J. Muga, *Physical review letters* **105**, 123003 (2010).
 - [28] J.-L. Wu, X. Ji, and S. Zhang, *Optics Express* **25**, 21084 (2017).
 - [29] K. Kumar, A. Vepsäläinen, S. Danilin, and G. Paraoanu, *Nature communications* **7**, 10628 (2016).
 - [30] N. N. Hegade, K. Paul, Y. Ding, M. Sanz, F. Albarrán-Arriagada, E. Solano, and X. Chen, *Physical Review Applied* **15**, 024038 (2021).
 - [31] Z. Yin, C. Li, J. Allcock, Y. Zheng, X. Gu, M. Dai, S. Zhang, and S. An, *Nature Communications* **13**, 188 (2022).
 - [32] T. Liu, F. Zhao, P. Lu, Q. Lao, X. Rao, M. Ding, J. Bian, F. Zhu, and L. Luo, *New Journal of Physics* **27**, 023023 (2025).
 - [33] N. Vitanov, K. Suominen, and B. Shore, *Journal of Physics B: Atomic, Molecular and Optical Physics* **32**, 4535 (1999).
 - [34] P. Marte, P. Zoller, and J. L. Hall, *Physical Review A* **44**, R4118 (1991).
 - [35] A. Baksic, H. Ribeiro, and A. A. Clerk, *Physical review letters* **116**, 230503 (2016).
 - [36] W. Gordy and R. L. Cook, *Microwave Molecular Spectra*, 3rd ed., *Techniques of Chemistry*, Vol. 18 (John Wiley & Sons (Wiley-Interscience), New York, 1984) pp. xiv, 929.
 - [37] D. Patterson, M. Schnell, and J. M. Doyle, *Nature* **497**, 475 (2013).
 - [38] F. J. Lovas, D. F. Plusquellic, B. H. Pate, J. L. Neill, M. T. Muckle, and A. J. Remijan, *Journal of Molecular Spectroscopy* **257**, 82 (2009).
 - [39] R. S. Judson and H. Rabitz, *Physical review letters* **68**, 1500 (1992).
 - [40] P. Brumer and M. Shapiro, *Chemical Physics Letters* **126**, 541 (1986).
 - [41] C. P. Koch, M. Lemesko, and D. Sugny, *Reviews of Modern Physics* **91**, 035005 (2019).

APPENDIX A: DERIVATION OF THE INTERACTING HAMILTONIAN

Here, we present the derivation of the Hamiltonian in the interaction picture, $H_{int}(t) = e^{iH_0 t} H_1 e^{-iH_0 t}$, by substituting the explicit forms of H_0 and H_1 . For the transition $|1\rangle \Leftrightarrow |2\rangle$ with energy splitting ω_{12} , the dipole interaction term written as

$$H_{int}(t) = e^{iH_0 t} \left[\frac{\Omega_P(t)}{2} \left(e^{i(\omega_P t + \phi_P)} + e^{-i(\omega_P t + \phi_P)} \right) (|1\rangle\langle 2| + |2\rangle\langle 1|) \right] e^{-iH_0 t} \quad (A1)$$

$$H_{int}(t) = \frac{\Omega_P(t)}{2} \left[e^{i(\omega_P - \omega_{12})t} e^{i\phi_P} |1\rangle\langle 2| + e^{-i(\omega_P - \omega_{12})t} e^{-i\phi_P} |2\rangle\langle 1| \right]$$

Assume that the applied field is nearly resonant ($\omega_P \approx \omega_{12}$)

$$H_{int}(t) = \frac{\Omega_P(t)}{2} \left[e^{i\phi_P} |1\rangle\langle 2| + e^{-i\phi_P} |2\rangle\langle 1| \right] \quad (A2)$$

In the case of a $|2\rangle \Leftrightarrow |3\rangle$ transition characterized by an energy separation ω_{12} , the corresponding dipole interaction term becomes

$$H_{int}(t) = e^{iH_0 t} \left[\frac{\Omega_S(t)}{2} \left(e^{i(\omega_S t + \phi_S)} + e^{-i(\omega_S t + \phi_S)} \right) (|2\rangle\langle 3| + |3\rangle\langle 2|) \right] e^{-iH_0 t}$$

$$H_{int}(t) = \frac{\Omega_S(t)}{2} \left[e^{i(\omega_S t + (\omega_{12} - \omega_{13}))} e^{i\phi_S} |2\rangle\langle 3| + e^{-i(\omega_S t + (\omega_{12} - \omega_{13}))} e^{-i\phi_S} |3\rangle\langle 2| \right] \quad (A3)$$

Since $\omega_{12} - \omega_{13} \approx \omega_{23} \approx \omega_S$, the Hamiltonian $H_{int}(t)$ becomes

$$H_{int}(t) = \frac{\Omega_S(t)}{2} \left[e^{i\phi_S} |2\rangle\langle 3| + e^{-i\phi_S} |3\rangle\langle 2| \right] \quad (A4)$$

Similarly for the transition $|1\rangle \Leftrightarrow |3\rangle$ with energy splitting ω_{13} , the dipole interaction term takes the form

$$H_{int}(t) = e^{iH_0 t} \left[\frac{\Omega_Q(t)}{2} \left(e^{i(\omega_Q t + \phi_Q)} + e^{-i(\omega_Q t + \phi_Q)} \right) (|1\rangle\langle 3| + |3\rangle\langle 1|) \right] e^{-iH_0 t} \quad (A5)$$

$$H_{int}(t) = \pm \frac{\Omega_Q(t)}{2} \left[e^{i(\omega_Q t - \omega_{13})} e^{i\phi_Q} |1\rangle\langle 3| + e^{-i(\omega_Q t - \omega_{13})} e^{-i\phi_Q} |3\rangle\langle 1| \right]$$

Consider the applied field is nearly resonant ($\omega_Q \approx \omega_{13}$)

$$H_{int}(t) = \pm \frac{\Omega_Q(t)}{2} \left[e^{i\phi_Q} |1\rangle\langle 3| + e^{-i\phi_Q} |3\rangle\langle 1| \right] \quad (A6)$$

Finally, the Hamiltonian matrix in the basis set ($|1\rangle, |2\rangle, |3\rangle$) becomes

$$H_{int}(t) = \frac{1}{2} \begin{pmatrix} 0 & \Omega_P e^{i\phi_P} & \pm \Omega_Q e^{i\phi_Q} \\ \Omega_P e^{-i\phi_P} & 0 & \Omega_S e^{i\phi_S} \\ \pm \Omega_Q e^{-i\phi_Q} & \Omega_S e^{-i\phi_S} & 0 \end{pmatrix} \quad (A7)$$

APPENDIX B: QUANTUM GATES

I. Q -pulse

The Hamiltonian for Q -pulse only is

$$H_{im}(t) = \pm \frac{\Omega_Q(t)}{2} [e^{i\phi_Q} |00\rangle\langle 10| + e^{-i\phi_Q} |10\rangle\langle 00|] \quad (B1)$$

We use the tensor product rule: $|ab\rangle\langle cd| = (|a\rangle\langle c|)_{q_0} \otimes (|b\rangle\langle d|)_{q_1}$.

\Rightarrow

$$\begin{aligned} |00\rangle\langle 10| &= (|0\rangle\langle 1|)_{q_0} \otimes (|0\rangle\langle 0|)_{q_1} \\ |10\rangle\langle 00| &= (|1\rangle\langle 0|)_{q_0} \otimes (|0\rangle\langle 0|)_{q_1} \end{aligned}$$

Therefore

$$H_Q(t_i) = \pm \frac{\Omega_Q(t_i)}{2} [e^{i\phi_Q} (|0\rangle\langle 1|)_{q_0} \otimes (|0\rangle\langle 0|)_{q_1} + e^{-i\phi_Q} (|1\rangle\langle 0|)_{q_0} \otimes (|0\rangle\langle 0|)_{q_1}]. \quad (B2)$$

The total time evolution for Q -pulse using the first-order Trotter becomes

$$U_Q^{(i)} = \prod_{i=1}^m e^{-iH_Q(t_i) \delta t} \quad (B3)$$

The quantum circuit realization of the Q -pulse must incorporate the essential structure identified from $U_Q^{(i)}$.

- If $q_1 = |1\rangle$: the Hamiltonian terms vanish, nothing is applied, and the system evolves as: $I_{q_0} \otimes (|1\rangle\langle 1|)_{q_1}$.
- If $q_1 = |0\rangle$: we get a non-trivial evolution governed by the unitary $\exp\left\{-i\delta t \frac{\pm\Omega_Q(t_i)}{2} (e^{i\phi_Q} |0\rangle\langle 1| + e^{-i\phi_Q} |1\rangle\langle 0|)_{q_0}\right\} \otimes |0\rangle\langle 0|_{q_1}$, which corresponds to applying a controlled rotation: $R_{\vec{n}}(\theta_i) = e^{-i\frac{\theta_i}{2}(n_x X + n_y Y)}$ where $\vec{n} = (\cos \phi_Q, \sin \phi_Q, 0)$ and $\theta_i = \Omega_Q(t_i) \delta t$.

By combining both results, we obtain

$$U_Q^{(i)} = e^{-i(H_Q(t_i)\delta t)} = I_{q_0} \otimes (|1\rangle\langle 1|)_{q_1} + R_{\vec{n}}(\theta_i) \otimes |0\rangle\langle 0|_{q_1} \quad (B4)$$

The Q -pulse quantum circuit implemented in Qiskit confirms this behavior, as illustrated in Fig. 2.

II. P - and S -pulse gate

For P -pulse the Hamiltonian $H_P(t)$ is

$$H_P(t) = \frac{\Omega_P(t)}{2} (|00\rangle\langle 11| + |11\rangle\langle 00|) \quad (B5)$$

$$H_P(t) = \frac{\Omega_P(t)}{2} (|0\rangle\langle 1|_{q_0} \otimes |0\rangle\langle 1| + |1\rangle\langle 0|_{q_1}) \quad (B6)$$

By Definition $|0\rangle\langle 1| + |1\rangle\langle 0|_{q_1} = X$. Putting the value of X in Eq. (B6)

$$H_P(t) = \frac{\Omega_P(t)}{2} (|0\rangle\langle 1|_{q_0} \otimes X_{q_1}) \quad (B7)$$

However, the controlled rotation can be implemented using a $(CX - Rx - CX)$ sequence, as illustrated in Fig. 2. For S -pulse, the Hamiltonian $H_S(t)$ is

$$H_S(t) = \frac{\Omega_S(t)}{2} (|11\rangle\langle 10| + |10\rangle\langle 11|) \quad (\text{B8})$$

Using identity $|11\rangle\langle 10| + |10\rangle\langle 11| = 2(\sigma_0^+ \sigma_1^- + \sigma_0^- \sigma_1^+) = \frac{1}{2}(X \otimes X + Y \otimes Y)$. Putting the value of identity in Eq. (B8)

$$H_S(t) = \frac{\Omega_S(t)}{4} (X \otimes X + Y \otimes Y)$$

The time evolution over a time interval δt become

$$U_S^{(i)} = e^{-i(H_S(t_i)\delta t)} = e^{-i\left[\frac{\Omega_S(t_i)}{4}(X \otimes X + Y \otimes Y)\right]\delta t}$$

we can further define XX and YY rotational gates with $\theta_i = \frac{\Omega_S(t_i)}{4}\delta t$

$$U_S^{(i)} = e^{-i\left[\frac{\Omega_S(t_i)}{4}(X \otimes X)\right]\delta t} \cdot e^{-i\left[\frac{\Omega_S(t_i)}{4}(Y \otimes Y)\right]\delta t} \quad (\text{B9})$$

APPENDIX C: DERIVATION OF EQUATION

$$U_0(t) = \sum_{n=0,\pm} |\gamma_n\rangle\langle \gamma_n(t)| \quad (\text{C1})$$

$$H_I(t) = U_0(t)H_{PS}(t)U_0^\dagger(t) - iU_0(t)\dot{U}_0^\dagger(t) \quad (\text{C2})$$

(i) $U_0(t)H_{PS}(t)U_0^\dagger(t)$:

$$\begin{aligned} U_0(t)H_{PS}(t)U_0^\dagger(t) &= \left[\sum_{n=0,\pm} |\gamma_n\rangle\langle \gamma_n(t)| \right] \left[\Omega_P(t)|00\rangle\langle 01| + \Omega_S(t)|01\rangle\langle 10| \right] \\ &\times \left[\sum_{n=0,\pm} |\gamma_n(t)\rangle\langle \gamma_n| \right] - i \left[\sum_{n=0,\pm} |\gamma_n\rangle\langle \gamma_n(t)| \left(\sum_{m=0,\pm} \frac{\partial}{\partial t} |\gamma_m(t)\rangle\langle \gamma_m| \right) \right] \end{aligned} \quad (\text{C3})$$

$$\begin{aligned} U_0(t)H_{PS}(t)U_0^\dagger(t) &= \left[|\gamma_+\rangle\langle \gamma_+(t)| + |\gamma_-\rangle\langle \gamma_-(t)| \right] \\ &\times \left[\Omega_P(t)|00\rangle\langle 01| + \Omega_S(t)|01\rangle\langle 10| + \text{h.c.} \right] \left[|\gamma_+(t)\rangle\langle \gamma_+| + |\gamma_-(t)\rangle\langle \gamma_-| \right] \end{aligned} \quad (\text{C4})$$

$$U_0(t)H_{PS}(t)U_0^\dagger(t) = \frac{\Omega_P^2(t)}{2\Omega} |\gamma_+\rangle\langle \gamma_+| + \frac{\Omega_S^2(t)}{2\Omega} |\gamma_-\rangle\langle \gamma_-|$$

$$U_0(t)H_{PS}(t)U_0^\dagger(t) = \Omega(t) \left[|\gamma_+\rangle\langle \gamma_+| - |\gamma_-\rangle\langle \gamma_-| \right] \quad (\text{C5})$$

For nonadiabatic coupling

$$-iU_0(t)\dot{U}_0^\dagger(t) = -i \left[|\gamma_+\rangle\langle \gamma_+(t)| \frac{\partial}{\partial t} |\gamma_+(t)\rangle\langle \gamma_+| + |\gamma_-\rangle\langle \gamma_-(t)| \frac{\partial}{\partial t} |\gamma_-(t)\rangle\langle \gamma_-| \right] \quad (\text{C6})$$

$$\frac{\partial}{\partial t} |\gamma_0(t)\rangle = -\dot{\alpha}_1 \sin \alpha_1(t) |00\rangle + \dot{\alpha}_1 \cos \alpha_1(t) |10\rangle$$

\Rightarrow

$$-iU_0(t)\dot{U}_0^\dagger(t) = \frac{\dot{\alpha}_1(t)}{\sqrt{2}} [|\gamma_+\rangle\langle\gamma_0| + |\gamma_-\rangle\langle\gamma_0|] \quad (C7)$$

The equation becomes

$$H_I(t) = \Omega(t) [|\gamma_+\rangle\langle\gamma_+| - |\gamma_-\rangle\langle\gamma_-|] + \frac{\dot{\alpha}_1(t)}{\sqrt{2}} [|\gamma_+\rangle\langle\gamma_0| + |\gamma_-\rangle\langle\gamma_0|] + \text{h.c.} \quad (C8)$$

APPENDIX D: COUNTERDIABATIC FRAME

The goal of STAP is to cancel nonadiabatic transitions by introducing a counteradiabatic auxiliary field $\Omega'_P(t)$ and $\Omega'_S(t)$, and the Hamiltonian takes the form

$$H'(t) = [\Omega_P(t) + \Omega'_P(t)] |00\rangle\langle 01| + [\Omega_S(t) + \Omega'_S(t)] |01\rangle\langle 10| + \text{h.c.} \quad (D1)$$

By applying $U_1(t) = \sum_{n=0,\pm} |\varphi_n\rangle\langle\varphi_n(t)|$ to $H'(t)$ the system is expressed in the adiabatic frame

$$H'_{\text{AD}}(t) = U_1(t)H'(t)U_1^\dagger(t) - iU_1(t)\dot{U}_1^\dagger(t) \quad (D2)$$

(i) $U_1(t)H'(t)U_1^\dagger(t)$:

$$U_1(t)H'(t)U_1^\dagger(t) = \left[\sum_{n=0,\pm} |\varphi_n\rangle\langle\varphi_n(t)| \right] \left[(\Omega_P(t) + \Omega'_P(t)) |00\rangle\langle 01| + (\Omega_S(t) + \Omega'_S(t)) |01\rangle\langle 10| + \text{h.c.} \right] \left[\sum_{n=0,\pm} |\varphi_n(t)\rangle\langle\varphi_n| \right] \quad (D3)$$

$$\begin{aligned} U_1(t)H'(t)U_1^\dagger(t) &= [|\varphi_+\rangle\langle\varphi_+(t)| + |\varphi_-\rangle\langle\varphi_-(t)|] \\ &\times [(\Omega_P(t) + \Omega'_P(t)) |00\rangle\langle 01| + (\Omega_S(t) + \Omega'_S(t)) |01\rangle\langle 10|] [|\varphi_+(t)\rangle\langle\varphi_+| + |\varphi_-(t)\rangle\langle\varphi_-|] \end{aligned} \quad (D4)$$

$$= \frac{1}{2}(\Omega_P(t) + \Omega'_P(t)) [-\sin \alpha_1(t) \cos \alpha_2(t) - i \sin \alpha_2(t) \cos \alpha_1(t) \cos \alpha_2(t)] |\varphi_+\rangle\langle\varphi_+| +$$

$$\frac{1}{2}(\Omega_P(t) + \Omega'_P(t)) [\sin \alpha_1(t) \cos \alpha_2(t) - i \sin \alpha_2(t) \cos \alpha_1(t) \cos \alpha_2(t)] |\varphi_-\rangle\langle\varphi_-| +$$

$$\frac{1}{2}(\Omega_S(t) + \Omega'_S(t)) [\cos \alpha_1(t) \cos \alpha_2(t) + i \sin \alpha_2(t) \sin \alpha_1(t) \cos \alpha_2(t)] |\varphi_+\rangle\langle\varphi_+| +$$

$$\frac{1}{2}(\Omega_S(t) + \Omega'_S(t)) [-\cos \alpha_1(t) \cos \alpha_2(t) - i \sin \alpha_2(t) \sin \alpha_1(t) \cos \alpha_2(t)] |\varphi_-\rangle\langle\varphi_-|$$

Solving the real part first

$$= \frac{1}{2} \left[\left\{ \left(\Omega_P(t) + \Omega'_P(t) \right) \left(-\sin \alpha_1(t) \right) \right\} + \left\{ \left(\Omega_S(t) + \Omega'_S(t) \right) \left(\cos \alpha_1(t) \right) \right\} \right] \cos \alpha_2(t) |\varphi_+\rangle \langle \varphi_+|$$

$$+ \frac{1}{2} \left[\left\{ \left(\Omega_P(t) + \Omega'_P(t) \right) \left(\sin \alpha_1(t) \right) \right\} + \left\{ \left(\Omega_S(t) + \Omega'_S(t) \right) \left(-\cos \alpha_1(t) \right) \right\} \right] \cos \alpha_2(t) |\varphi_-\rangle \langle \varphi_-|$$

$$U_1(t)H'(t)U_1^\dagger(t) = Y(t) \left[|\varphi_+\rangle \langle \varphi_+| - |\varphi_-\rangle \langle \varphi_-| \right]$$

where $Y(t) = \left[\Omega'_S(t) \cos \alpha_1(t) - \Omega'_P(t) \sin \alpha_1(t) + \Omega \cos 2\alpha_1(t) \right] \cos \alpha_2(t)$.

Solving the imaginary part

$$\frac{1}{2} \left[\left(\Omega_P(t) + \Omega'_P(t) \right) \left(-\sin \alpha_2(t) \cos \alpha_1(t) \right) + \left(\Omega_S(t) + \Omega'_S(t) \right) \left(i \sin \alpha_2(t) \sin \alpha_1(t) \right) \right] \cos \alpha_2(t) |\varphi_+\rangle \langle \varphi_+|$$

$$+ \frac{1}{2} \left[\left(\Omega_P(t) + \Omega'_P(t) \right) \left(-\sin \theta_2(t) \cos \alpha_1(t) \right) + \left(\Omega_S(t) + \Omega'_S(t) \right) \left(-i \sin \theta_2(t) \sin \alpha_1(t) \right) \right] \cos \theta_2(t) |\varphi_-\rangle \langle \varphi_-|$$

After including the h.c. terms, the contributions cancel, and the imaginary part vanishes. Thus, $U_1(t)H'(t)U_1^\dagger(t)$ becomes

$$U_1(t)H'(t)U_1^\dagger(t) = Y(t) \left[|\varphi_+\rangle \langle \varphi_+| - |\varphi_-\rangle \langle \varphi_-| \right]$$

Now, we calculate $iU(t)\dot{U}^\dagger(t)$

$$iU(t)\dot{U}^\dagger(t) = \left[\sum_{n=0,\pm} |\varphi_n\rangle \langle \varphi_n(t)| \right] \frac{\partial}{\partial t} \left[\sum_{n=0,\pm} |\varphi_n(t)\rangle \langle \varphi_n| \right] \quad (\text{D5})$$

$$iU(t)\dot{U}^\dagger(t) = \left[|\varphi_+(t)\rangle \langle \varphi_+(t)| \right] \frac{\partial}{\partial t} \left[|\varphi_0(t)\rangle \langle \varphi_0| \right] + \left[|\varphi_-(t)\rangle \langle \varphi_-(t)| \right] \frac{\partial}{\partial t} \left[|\varphi_0(t)\rangle \langle \varphi_0| \right] \quad (\text{D6})$$

$$\frac{\partial}{\partial t} |\varphi_0(t)\rangle = \dot{\alpha}_2 \sin \alpha_2(t) \left[\cos \alpha_1(t) |00\rangle + \sin \alpha_1(t) \dot{\alpha}_2 |10\rangle \right] + \cos \alpha_2(t) \left[-\dot{\alpha}_1(t) \sin \alpha_1(t) |00\rangle + \dot{\alpha}_1(t) \cos \alpha_1(t) |10\rangle \right]$$

$$+ e^{i\phi} \dot{\alpha}_2 \cos \alpha_2(t) |11\rangle$$

$$\langle \varphi_+(t) | \frac{\partial}{\partial t} | \varphi_0(t) \rangle = \frac{1}{\sqrt{2}} \left[\left\{ \left(\sin \alpha_1(t) + i \sin \alpha_2(t) \cos \alpha_1(t) \right) \right\} \langle 00| + \cos \alpha_2(t) \langle 11| - \left\{ \left(\cos \alpha_1(t) + i \sin \alpha_2(t) \sin \alpha_1(t) \right) \right\} \langle 10| \right]$$

$$\left[-\dot{\alpha}_2 \sin \alpha_2(t) \left\{ \left(\cos \alpha_1(t) |00\rangle + \sin \alpha_1(t) |10\rangle \right) \right\} + \cos \alpha_2(t) \left\{ \left(-\dot{\alpha}_1 \sin \alpha_1(t) |00\rangle + \dot{\alpha}_1 \cos \alpha_1(t) |10\rangle \right) \right\} + e^{i\phi} \dot{\alpha}_1 \cos \alpha_2(t) |11\rangle \right]$$

$$= \frac{1}{\sqrt{2}} \left[\left\{ \sin \alpha_1 + i \sin \alpha_2 \cos \alpha_1 \right\} \left\{ -\dot{\alpha}_2 \sin \alpha_2 \cos \alpha_1 \right\} + \left\{ \sin \alpha_1 + i \sin \alpha_2 \cos \alpha_1 \right\} \left\{ -\cos \alpha_2 \dot{\alpha}_1 \sin \alpha_1 \right\} - \cos^2 \alpha_2 e^{i\phi} \right]$$

$$\begin{aligned}
& - \left\{ \cos \alpha_1 - i \sin \alpha_2 \sin \alpha_1 \right\} \left\{ -\dot{\alpha}_2 \sin \alpha_2 \sin \alpha_1 \right\} - \left\{ \cos \alpha_1 - i \sin \alpha_2 \sin \alpha_1 \right\} \left\{ \cos \alpha_2 \dot{\alpha}_1 \cos \alpha_1 \right\} \\
& = \frac{1}{\sqrt{2}} \left[-\dot{\alpha}_2 \sin \alpha_1 \sin \alpha_2 \cos \alpha_1 - i \dot{\alpha}_2 \sin^2 \alpha_2 \cos^2 \alpha_1 - \dot{\alpha}_1 \sin^2 \alpha_1 \cos \alpha_2 \right. \\
& \quad \left. - i \dot{\alpha}_1 \sin \alpha_1 \sin \alpha_2 \cos \alpha_1 \cos \alpha_2 - e^{i\phi} \dot{\alpha}_2 \cos^2 \alpha_2 + \dot{\alpha}_2 \sin \alpha_1 \sin \alpha_2 \cos \alpha_1 \right. \\
& \quad \left. - i \dot{\alpha}_2 \sin^2 \alpha_2 \sin^2 \alpha_1 - \dot{\alpha}_1 \cos^2 \alpha_1 \cos \alpha_2 + i \dot{\alpha}_1 \cos \alpha_1 \cos \alpha_2 \sin \alpha_1 \sin \alpha_2 \right] \\
& = -\frac{1}{\sqrt{2}} \left[\dot{\alpha}_2 \sin \alpha_1 \sin \alpha_2 \cos \alpha_1 + \dot{\alpha}_1 \sin^2 \alpha_1 \cos \alpha_2 \right] - \frac{i}{\sqrt{2}} \left[\dot{\alpha}_2 \sin^2 \alpha_2 \cos^2 \alpha_1 + \dot{\alpha}_1 \sin \alpha_1 \sin \alpha_2 \cos \alpha_1 \cos \alpha_2 \right] \\
& = \frac{i}{\sqrt{2}} \left[e^{i\phi} \dot{\alpha}_2 \cos^2 \alpha_2 \right] + \frac{1}{\sqrt{2}} \left[\dot{\alpha}_2 \sin \alpha_1 \sin \alpha_2 \cos \alpha_1 - \dot{\alpha}_1 \cos^2 \alpha_1 \cos \alpha_2 \right] \\
& \quad + \frac{i}{\sqrt{2}} \left[\dot{\alpha}_2 \sin^2 \alpha_2 \sin^2 \alpha_1 + \dot{\alpha}_1 \cos \alpha_1 \cos \alpha_2 \sin \alpha_1 \sin \alpha_2 \right]
\end{aligned}$$

Solving the real part first

$$\begin{aligned}
& = -\frac{1}{\sqrt{2}} \left[\dot{\alpha}_2 \sin \alpha_1 \sin \alpha_2 \cos \alpha_1 + \dot{\alpha}_1 \sin^2 \alpha_1 \cos \alpha_2 \right] + \frac{1}{\sqrt{2}} \left[\dot{\alpha}_2 \sin \alpha_1 \sin \alpha_2 \cos \alpha_1 - \dot{\alpha}_1 \cos^2 \alpha_1 \cos \alpha_2 \right] \\
& = \frac{1}{\sqrt{2}} \dot{\alpha}_1 \cos \alpha_2 \left[\sin^2 \alpha_1 + \cos^2 \alpha_1 \right] \\
& = \frac{1}{\sqrt{2}} \dot{\alpha}_1 \cos \alpha_2 \tag{D7}
\end{aligned}$$

Solving the imaginary part

$$\begin{aligned}
& = -\frac{i}{\sqrt{2}} \left[\dot{\alpha}_2 \sin^2 \alpha_2 \cos^2 \alpha_1 + \dot{\alpha}_1 \sin \alpha_1 \sin \alpha_2 \cos \alpha_1 \cos \alpha_2 \right] \\
& \quad - \frac{i}{\sqrt{2}} \left[e^{i\phi} \dot{\alpha}_2 \cos^2 \alpha_2 \right] + \frac{i}{\sqrt{2}} \left[\dot{\alpha}_2 \sin^2 \alpha_2 \sin^2 \alpha_1 + \dot{\alpha}_1 \cos \alpha_1 \cos \alpha_2 \sin \alpha_1 \sin \alpha_2 \right] \\
& = \frac{i}{\sqrt{2}} \left[-\dot{\alpha}_2 \sin^2 \alpha_2 (\cos^2 \alpha_1 + \sin^2 \alpha_1) - \dot{\alpha}_2 \cos^2 \alpha_2 + 2\dot{\alpha}_1 \sin \alpha_2 \sin \alpha_1 \cos \alpha_1 \cos \alpha_2 \right] \\
& = \frac{i}{\sqrt{2}} \left[+\dot{\alpha} \sin^2 \alpha_2 \cos 2\alpha_1 - \dot{\alpha}_2 \cos^2 \alpha_2 + \dot{\alpha}_1 \sin \alpha_2 \sin 2\alpha_1 \cos \alpha_2 \right] \\
& \Rightarrow \\
& -i \langle \varphi_+(t) | \dot{\varphi}_0(t) \rangle = \frac{1}{\sqrt{2}} \left[i \dot{\alpha}_1 \cos \alpha_2 + \dot{\alpha}_2 \sin^2 \alpha_2 \cos 2\alpha_1 - \dot{\alpha}_2 \cos^2 \alpha_2 + \dot{\alpha}_1 \sin \alpha_1 \sin 2\alpha_2 \cos \alpha_2 \right]
\end{aligned}$$

$$-i\langle\varphi_+(t)|\dot{\varphi}_0(t)\rangle = \frac{1}{\sqrt{2}} \left[\dot{\alpha}_1 \{i \cos \alpha_2 + \sin \alpha_1 \sin 2\alpha_2 \cos \alpha_2\} + \dot{\theta}_2 \{\sin^2 \alpha_2 \cos 2\alpha_1 - \cos^2 \alpha_2\} \right] \quad (\text{D8})$$

Combining Eq.(D7) and Eq. (D8), we get

$$iU(t)\dot{U}^\dagger(t) = [\lambda_+(t) |\varphi_+(t)\rangle \langle\varphi_0(t)| + \lambda_-(t) |\varphi_-(t)\rangle \langle\varphi_0(t)| + \text{h.c.}] \quad (\text{D9})$$

where

$$\begin{aligned} \lambda_\pm(t) = i \bigg\{ & \dot{\alpha}_1(t) \cos \alpha_2(t) - \sin \theta_2(t) [\Omega'_S(t) \cos \alpha_1(t) - \Omega'_P(t) \sin \alpha_1(t) + \Omega \cos 2\alpha_1(t)] \bigg\} \\ & \mp [\Omega'_P(t) \cos \alpha_1(t) - \Omega'_S(t) \sin \alpha_1(t) + \Omega \sin 2\alpha_1(t) + \dot{\alpha}_2(t)] \end{aligned}$$